Version of Record: https://www.sciencedirect.com/science/article/pii/S0034425720300985
Manuscript_be2590912ee4e81ad54e5c4dc08f75ce

Satellite footprint data from OCO-2 and TROPOMI reveal significant spatio-temporal and inter-vegetation type variabilities of solar-induced fluorescence yield in the U.S. Midwest

Cong Wang[1]*, Kaiyu Guan[1,2]*, Bin Peng[1,2], Min Chen[3], Chongya Jiang[1,4], Yelu Zeng[5], Genghong Wu[1], Sheng Wang[1], Jin Wu[6], Xi Yang[7], Christian Frankenberg[8,9], Philipp Köhler[8], Joseph Berry[5], Carl Bernacchi[4,10,11], Kai Zhu[12], Caroline Alden[13,14], and Guofang Miao[1]

1 College of Agricultural, Consumer and Environmental Sciences, University of Illinois at Urbana Champaign, USA

[2] National Center for Supercomputing Applications, University of Illinois at Urbana-Champaign, USA

[3] Joint Global Change Research Institute, Pacific Northwest National Laboratory, College Park, MD, USA

[4] Carl R. Woese Institute for Genomic Biology, University of Illinois at Urbana-Champaign, Urbana, IL, USA

[5] Department of Global Ecology, Carnegie Institution for Science, Stanford, CA, USA

[6] Department of Environmental and Climatic Sciences, Brookhaven National Laboratory, Upton, NY, USA

[7] Department of Environmental Sciences, University of Virginia, Charlottesville, VA, USA

[8] Division of Geological and Planetary Sciences, California Institute of Technology, Pasadena, CA, USA

[9] Jet Propulsion Laboratory, California Institute of Technology, Pasadena, CA, USA

[10] Department of Plant Biology, University of Illinois at Urbana-Champaign, Urbana, IL, USA

[11] USDA ARS Global Change and Photosynthesis Research Unit, Urbana, IL, USA

[12] Department of Environmental Studies, University of California, Santa Cruz, CA, USA

[13] Cooperative Institute for Research in Environmental Sciences, University of Colorado Boulder, Boulder, CO, USA

[14] NOAA/ESRL Global Monitoring Division, Boulder, CO, USA

* Corresponding author: Kaiyu Guan and Cong Wang

E-mail address: kaiyug@illinois.edu (Kaiyu Guan) and wangcongrs@gmail.com (Cong Wang)

Abstract:

Solar-induced chlorophyll fluorescence (SIF) measured from space has been increasingly used to quantify plant photosynthesis at regional and global scales. Apparent canopy SIF yield ($SIF_{yield\ apparent}$), determined by fluorescence yield (Φ_F) and escaping ratio (f^{esc}), together with absorbed photosynthetically active radiation (APAR), is crucial in driving spatio-temporal variability of SIF. While strong linkages between $SIF_{yield\ apparent}$ and plant physiological responses and canopy structure have been suggested, spatio-temporal variability of $SIF_{yield\ apparent}$ at regional scale remains largely unclear, which limits our understanding of the spatio-temporal variability of SIF and its relationship with photosynthesis. In this study, we utilized recent SIF data with high spatial resolution from two satellite instruments, OCO-2 and TROPOMI, together with multiple other datasets. We estimated $SIF_{yield\ apparent}$ across space, time, and different vegetation types in the U.S. Midwest during crop growing season (May to September) from 2015-2018. We found that $SIF_{yield\ apparent}$ of croplands was larger than non-croplands during peak season (July-August). However, $SIF_{yield\ apparent}$ between corn (C4 crop) and soybean (C3 crop) did not show a significant difference. $SIF_{yield\ apparent}$ of corn, soybean, forest, and grass/pasture show clear seasonal and spatial patterns. The spatial variability of precipitation during the growing season could explain the overall spatial pattern of $SIF_{yield\ apparent}$. Further analysis by decomposing $SIF_{yield\ apparent}$ into Φ_F and f^{esc} using near-infrared reflectance of vegetation (NIR_V) suggests that f^{esc} may be the major driver of the observed variability of $SIF_{yield\ apparent}$.

Keywords: solar-induced chlorophyll fluorescence, OCO-2, TROPOMI, fluorescence yield, croplands, NIR_V, escaping ratio

1. Introduction

Accurate and timely estimation of ecosystem photosynthesis measured as gross primary production (GPP) is crucial for understanding carbon exchange between the biosphere and atmosphere (Beer et al., 2010). GPP also largely determines vegetation net primary productivity and crop yield (Guan et al., 2016; Guanter et al., 2014). Satellite measurements of solar-induced chlorophyll fluorescence (SIF) are increasingly used to approximate GPP variability across large spatial and temporal scales (Frankenberg et al., 2011; Guan et al., 2016; Joiner et al., 2011; MacBean et al., 2018; Shiga et al., 2018). A number of studies have shown either linear or nonlinear relationships between GPP and canopy SIF at different spatial and temporal scales and from various sensors (Li et al., 2018a; Smith et al., 2018; Verma et al., 2017; Zuromski et al., 2018; Damm et al., 2015; Zhang et al., 2016). However, fundamental controls of large-scale variabilities in SIF remain unclear.

The widely-used light use efficiency (LUE)-based GPP model (Monteith, 1972) can be adapted to express SIF at the top of canopy (Guanter et al., 2014):

$$GPP = PAR \times fPAR \times LUE = APAR \times LUE \tag{1}$$

and

$$\begin{aligned} SIF &= PAR \times fPAR \times SIF_{apparent\ yield} \\ &= APAR \times SIF_{apparent\ yield} = APAR \times \Phi_F \times f^{esc} \end{aligned} \tag{2}$$

where PAR is photosynthetically active radiation, fPAR is the fraction of absorbed photosynthetically active radiation, APAR is absorbed PAR and LUE is light use efficiency at which APAR is used in photosynthesis. Apparent canopy SIF yield ($\mathrm{SIF}_{\mathrm{yield\ apparent}}$) can be defined as SIF observed in the direction of the sensor per PAR absorbed by canopies. $SIF_{yield\ apparent}$ is jointly determined by fluorescence yield (Φ_F) and escaping ratio (f^{esc}, Liu et al., 2018; Yang and van der Tol, 2018; Zeng et al., 2019; Du et al., 2017). Empirical studies have reported correlations between LUE and $SIF_{yield\ apparent}$ (Yang et al., 2017; Yang et al., 2015), and linkage between $SIF_{yield\ apparent}$ and plant physiological response (Song et al, 2018). Based on Equation 2, both APAR and $SIF_{yield\ apparent}$ contribute to overall SIF variability. Although some studies find a strong dominance of APAR in SIF (e.g. Miao et al., 2018; Yang et al., 2018), $SIF_{yield\ apparent}$ variation is what distinguishes SIF from APAR. Significant efforts have been made to derive PAR and fPAR from satellite remote sensing and ground-based observations (Ryu et al., 2018; Tian, 2004), yet characterization and understanding of $SIF_{yield\ apparent}$ remain much less studied. Existing studies have shown that $SIF_{yield\ apparent}$ can vary with vegetation type, plant age, growth stage, and growth conditions (Colombo et al., 2018; Miao et al., 2018; Sun et al., 2015). Additionally, there are indications of considerable spatio-temporal variations of $SIF_{yield\ apparent}$ (Joiner et al., 2011; Li et al., 2018b). However, understanding of $SIF_{yield\ apparent}$ variability over large spatial and temporal scales is insufficient, and the knowledge gap in $SIF_{yield\ apparent}$ over spatio-temporal scales is an outstanding source of uncertainty that limits our current understanding of SIF variability.

Various satellite-based SIF sensors have emerged in the past decade and derived SIF products have progressed from coarse resolutions in space and time to finer resolution. The first global SIF product from Greenhouse Gases Observing Satellite (GOSAT, Frankenberg et al., 2011; Guanter et al., 2012; Joiner et al., 2011), and the subsequent products from Global Ozone Monitoring Experiment-2 (GOME-2, Joiner et al., 2013; Köhler et al., 2015) and

SCanning Imaging Absorption spectroMeter for Atmospheric CHartographY (SCIAMACHY, Joiner et al., 2012; Köhler et al., 2015) provide an important opportunity to evaluate $SIF_{yield\ apparent}$ over large spatio-temporal scales (Joiner et al., 2011). However, due to coarse resolutions of those SIF products (0.5° or coarser for gridded data) and associated intra-pixel mixing effects, the accuracy of $SIF_{yield\ apparent}$ estimation at the vegetation-type level is limited. Launched on July 2, 2014, Orbiting Carbon Observatory-2 (OCO-2) retrieves SIF at a significantly improved spatial resolution compared with previous SIF products, though the spatial coverage is sparse (Frankenberg et al., 2014). The spatial resolution of an OCO-2 footprint is approximately 1.3×2.25 km^2. Recent studies have compared and validated OCO-2 SIF products with GPP measurements from eddy covariance (EC) flux towers, given the comparable spatial footprints between GPP and SIF measurements (Li et al., 2018c; Lu et al., 2018). Additionally, a new SIF product based on TROPOspheric Monitoring Instrument (TROPOMI) was released in 2018 (Köhler et al., 2018). TROPOMI measures SIF at both high spatial resolution and high temporal frequency, with a footprint of 3.5×7 km^2 at nadir and almost daily coverage. The two high-spatial-resolution SIF datasets, OCO-2 and TROPOMI, have the potential to provide more accurate assessments of $SIF_{yield\ apparent}$ for specific vegetation types.

The U.S. Midwest Corn Belt currently produces more than 30% of global corn and soybean (USDA, 2018), and has been identified as a global SIF hotspot during the boreal summer (Guanter et al., 2014). Therefore, a better understanding of the controls on SIF would likely lead to a better quantification of regional carbon budgets and improved prediction of crop productivity (Guan et al., 2016). To understand controls of SIF variations, estimating

$SIF_{yield\ apparent}$ for each vegetation type is necessary because $SIF_{yield\ apparent}$ can vary substantially between different vegetation types in this area. First, the $SIF_{yield\ apparent}$ of croplands is likely larger than that of non-croplands since SIF in the U.S. Corn Belt is remarkably high during crop growing season (Guanter et al., 2014). Second, within croplands, the GPP of corn is usually much larger than that of soybean (Joo et al., 2016; Suyker and Verma, 2012). This difference in photosynthesis could be attributed to canopy structure, for example, leaf area index (LAI) and leaf angle distribution (LAD), and plant physiology, both of which could potentially drive differences in $SIF_{yield\ apparent}$ (Frankenberg and Berry, 2018; Porcar-Castell et al., 2014). However, whether and how $SIF_{yield\ apparent}$ of corn and soybean differ is still not well studied. Finally, the non-crop vegetation types of forest and grass/pasture, for example, are also different in both physiological processes and canopy structures.

This study aims to provide a comprehensive analysis of the spatio-temporal variability of $SIF_{yield\ apparent}$ of vegetation in the U.S. Midwest. The two newest satellite SIF datasets, i.e. OCO-2 and TROPOMI footprint SIF observations, are used to provide a more accurate estimation of $SIF_{yield\ apparent}$ of specific vegetation types. Specifically, we aim to address the following questions: How does $SIF_{yield\ apparent}$ of croplands differ from $SIF_{yield\ apparent}$ of non-croplands during crop growing season? How does $SIF_{yield\ apparent}$ of corn (C4 crop) differ from $SIF_{yield\ apparent}$ of soybean (C3 crop)? What are seasonal and spatial patterns of $SIF_{yield\ apparent}$ of the four major vegetation types? What drives variability of $SIF_{yield\ apparent}$ in space, time, and across vegetation types?

2. Data and Methodology

2.1 Study region

The study region spans 15 states in the U.S. Midwest region (Fig. 1) including North Dakota, South Dakota, Nebraska, Kansas, Minnesota, Iowa, Missouri, Wisconsin, Illinois, Michigan, Indiana, Ohio, Kentucky, Wyoming (East to 107 °W), and Colorado (East to 107 °W). Corn and soybean are the major crop types in this area. In addition to crops, forest and grass/pasture are also dominant vegetation types in the U.S. Midwest. Forests are mainly distributed in the northeast, southeast, and west of the study area and grass/pasture is mainly distributed in the west (Fig. 1). Most forests are temperate deciduous, except for Ponderosa Pine in the west and Spruce/Fir in the north. In this study, we focused on the four main vegetation types: corn, soybean, forest, and grass/pasture.

2.2 Satellite SIF footprint data

We primarily used the OCO-2 SIF Lite product (v. B8100r), which contains bias-corrected SIF and other related fields for individual footprints on a daily basis (Sun et al., 2018). The data were obtained from (ftp://fluo.gps.caltech.edu/data/OCO2/sif_lite_B8100/).

The OCO-2 spectrometer measures high-resolution spectra in O_2-A band (757-775 nm, full width at half maximum = 0.042 nm) with a local overpass time at about 1:30 pm, which was utilized for OCO-2 SIF retrievals at 757 nm (SIF757) and 771 nm (SIF771) based on in-filling

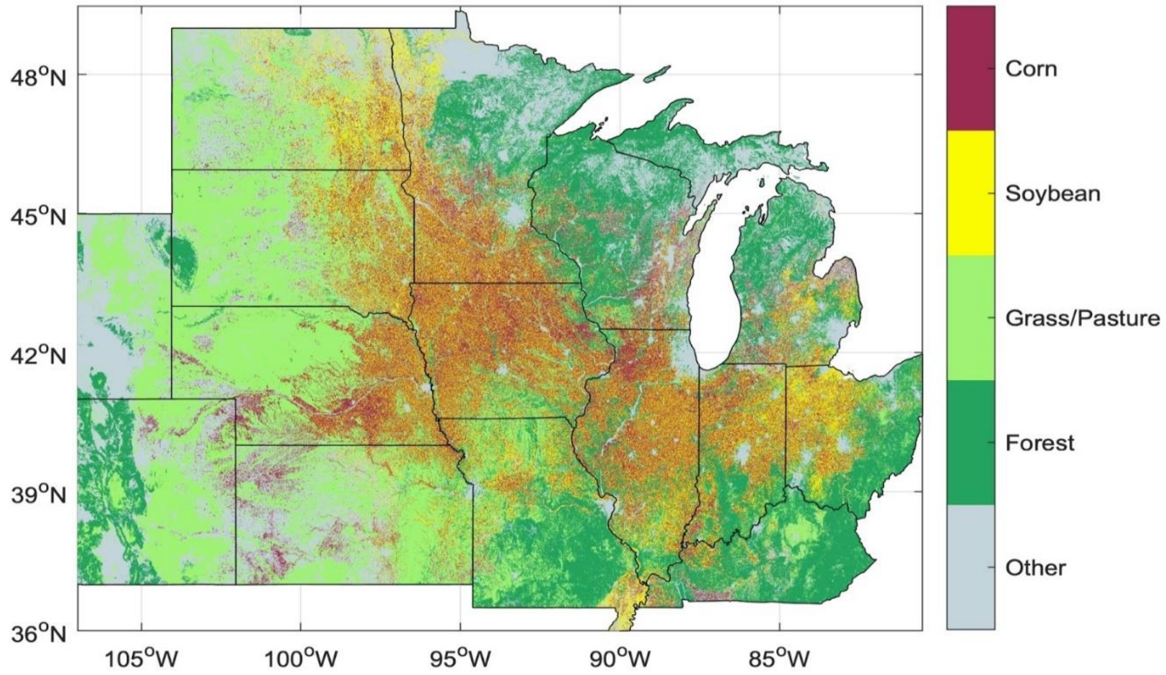

Fig. 1 Main vegetation types (i.e. corn, soybean, grass/pasture, and forest) in the U.S. Midwest, derived from Cropland Data Layer of 2015 for illustration.

of solar Fraunhofer lines (Frankenberg et al., 2014). SIF values used here were calculated as

(SIF757+1.5×SIF771)/2 because SIF771 is typically ~1.5 times lower than SIF757 (Sun et al., 2018). The nominal spatial resolution of a footprint is 1.3×2.25 km^2, with eight footprints along-track covering a 10.6 km-wide swath and a repeat cycle of approximately 16 days. SIF observations depend on viewing geometry (Z. Zhang et al., 2018) which for OCO-2 alternates mainly between nadir mode and glint mode. We only used measurements from nadir mode because of slightly higher spatial resolution, a better signal-to-noise ratio over land and more useful soundings in regions impacted by clouds and topography (Sun et al., 2018). We used only data during the crop growing season (May - September) from 2015 to 2018. Fig. 2a and 2b show a summary of the spatial and temporal coverage of OCO-2 footprints used in the study. The footprints were distributed along separated tracks with high data density in the west; fewer data were available in August and September in 2017.

In addition to OCO-2, we also used the latest released TROPOMI SIF footprint data

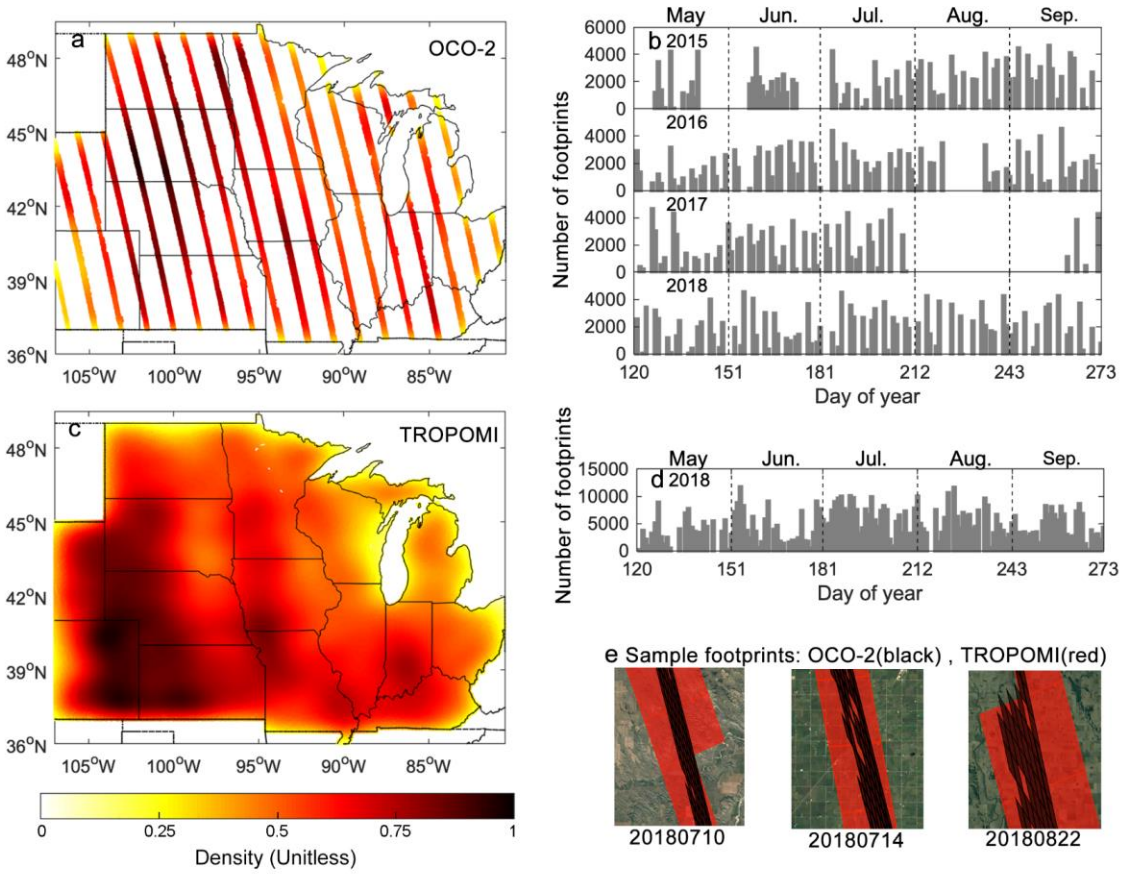

Fig. 2 Illustration of availability of OCO-2 and TROPOMI footprint data in both space and time. Panels (a) and (b) respectively represent the spatial coverage and frequency of observations over time for OCO-2 data from 2015 to 2018. Panels (c) and (d) are the spatial and temporal distributions of the number of the footprint of TROPOMI data in 2018. (e) shows three examples of the footprint of OCO-2 and TROPOMI. The color background shown in (a) and (c) represents the density of the footprint observations.

(ftp://fluo.gps.caltech.edu/data/tropomi/). The TROPOMI onboard Sentinel 5 Precursor satellite has a local overpass time at about 1:30 pm and a repeat cycle of 17 days, and provides spectra measurements in the near-infrared band (band 6, 727-775 nm, full width at half maximum = 0.38 nm), which makes SIF retrieval possible. A data-driven approach similar to previous studies (Guanter et al., 2015; Köhler et al., 2015) was employed to extract the SIF signal using spectral measurements ranging from 743 nm to 758 nm (Köhler et al., 2018). The nominal spatial resolution of a TROPOMI footprint is 7 km along track and 3.5-15 km across track, with a wide swath width of approximately 2,600 km. This wide swath allows almost daily global observations. We used available data from May to September in 2018 with cloud cover less than 0.3 and view zenith angle less than 10 degrees. Fig. 2e shows some examples of the selected TROPOMI footprints. Fig. 2c and 2d show a summary of the spatial and temporal availability of the total TROPOMI footprint observations used in the current study.

2.3 Estimating $\mathrm{SIF}_{\text{yield apparent}}$, Φ_F and f^{esc} at the satellite footprint level

In this section, we describe ancillary data and how we process these data to estimate $\mathrm{SIF}_{\text{yield apparent}}$, Φ_F, and f^{esc} at the satellite footprint level. $\mathrm{SIF}_{\text{yield apparent}}$ at the satellite footprint level is calculated according to Equation 2.

Estimating f^{esc} and Φ_F over a large scale is challenging. In this study, we employed the following equations according to a newly developed algorithm (Zeng et al, 2019):

$$f^{esc} \approx \frac{NIR_v}{fPAR} \tag{3}$$

$$\Phi_F \approx \frac{SIF}{PAR \times NIR_v} \tag{4}$$

$$\mathrm{NIR}_v = NIR \times NDVI = NIR \times \frac{NIR-Red}{NIR+Red} \tag{5}$$

where NIRv is near-infrared reflectance of vegetation, NIR and Red are reflectances of near-infrared and red bands. To calculate these variables, SIF data were obtained from OCO-2 and TROPOMI datasets as described in Section 2.2. Instantaneous PAR is the output product from Ryu et al., (2018). An artificial neural network surrogate model (Ryu et al., 2018), trained from a Monte Carlo ray-tracing model (Kobayashi and Iwabuchi, 2008) was used to produce the product. The model was driven by MODIS cloud optical thickness (3 km resolution), aerosol optical depth (1 km resolution), total water vapor (1 km resolution), total ozone (5 km resolution), and shortwave albedo products (1 km resolution), as well as GMTED2010 elevation product (1 km resolution). Detailed information about the model and data processing can be found in Ryu et al. (2018). Four fPAR datasets were used to estimate $\mathrm{SIF}_{\mathrm{yield\ apparent}}$. MCD15A2H from MODIS (Myneni et al., 2002) and VNP15A2H from VIIRS (Myneni and Knyazkhin 2018) are 8-day composite datasets with a spatial resolution of 500 m. PROBA-V GEOV1 fPAR data are delivered every 10 days with a spatial resolution of 300 m (Baret et al 2013). We calculated daily fPAR from the three temporal composited fPAR datasets using a simple linear interpolation. MCD43A4 provides daily Nadir Bidirectional Reflectance Distribution Function (BRDF)-Adjusted Reflectance data at a 500-meter resolution which were used to calculate NDVI. A simple NDVI-fPAR model was employed to generate the fourth fPAR estimation (Peng et al., 2012, Text S1). Only footprints with all the four fPAR values larger than 0.1 were included. $\mathrm{SIF}_{\mathrm{yield\ apparent}}$ was calculated independently with the four fPAR estimations. The averaged $\mathrm{SIF}_{\mathrm{yield\ apparent}}$ from the four estimations was finally used in the analysis. MCD43A4 was also used to calculate $\mathrm{NIR}_{\mathrm{V}}$.

2.4 Data analysis

We performed the following analysis to address the scientific questions raised in the introduction section. First, to detect the difference of $SIF_{yield\ apparent}$ between croplands (corn and soybean) and non-croplands, we examined relationships between the land cover fraction of croplands and $SIF_{yield\ apparent}$ at the satellite footprint level for both OCO-2 and TROPOMIover the entire study domain. The land cover fraction of different vegetation types was calculated from the USDA NASS Cropland Data Layer (CDL) dataset. A linear regression analysis was conducted for each month from May to September. The slope of the regression indicates a difference of $SIF_{yield\ apparent}$ between croplands and non-croplands; a positive slope means that $SIF_{yield\ apparent}$ of croplands is larger than that of non-croplands. We performed this analysis rather than directly comparing pure croplands and non-croplands footprints because most footprints contain mixed vegetation types.

Second, we selected cropland dominated footprints, defined as those footprints with a fraction of croplands greater than 80%. We then examined relationships between corn fraction of the total area in a footprint and $SIF_{yield\ apparent}$ to detect the difference of $SIF_{yield\ apparent}$ between corn and soybean. An increasing trend of $SIF_{yield\ apparent}$ with the increase of corn fraction indicates that the $SIF_{yield\ apparent}$ of corn is larger than soybean. The analysis was performed over the entire study area and also over three small sub-regions.

Spatial-temporal patterns of $SIF_{yield\ apparent}$ of different vegetation types were explored. Both f^{esc} and Φ_F can contribute to the spatial-temporal patterns and differences among vegetation types. We collected $SIF_{yield\ apparent}$ of OCO-2 footprints for which the fraction of a specific vegetation type is larger than 80%. For TROPOMI data, the threshold value of the fraction was set to 50% for corn and soybean because few footprints remained when the threshold value was set to 80%. The spatial patterns of $\mathrm{SIF}_{\mathrm{yield\ apparent}}$ of different vegetation types for each month were smoothed by averaging all available $\mathrm{SIF}_{\mathrm{yield\ apparent}}$ of the specific vegetation type within a 0.5°×0.5° grid. Seasonal patterns of $\mathrm{SIF}_{\mathrm{yield\ apparent}}$ were examined. The study area was divided into three sub-regions for each vegetation type according to spatial distributions of the footprints, and temporal dynamics of monthly mean $\mathrm{SIF}_{\mathrm{yield\ apparent}}$ were plotted for the three sub-regions.

Variability of $\mathrm{SIF}_{\mathrm{yield\ apparent}}$ could be driven by several potential factors. First, we examined impacts of air temperature and precipitation on $\mathrm{SIF}_{\mathrm{yield\ apparent,}}$ because these climate variables could affect $\mathrm{SIF}_{\mathrm{yield\ apparent}}$ through either f^{esc} or Φ_F. We plotted $\mathrm{SIF}_{\mathrm{yield\ apparent}}$ of each vegetation type in each growing season month within a climate space built by a multi-year average of monthly mean air temperature and monthly total precipitation. Mean air temperature and total precipitation for May to September were calculated from monthly PRISM Climate data with a spatial resolution of 4 km from 2015 to 2018 (http://prism.oregonstate.edu/, Daly et al., 2008). Second, we examined differences in $\mathrm{SIF}_{\mathrm{yield\ apparent}}$ between grass and pasture, and among different forest types which could also arise from f^{esc} and Φ_F. The USGS National Land Cover Database (NLCD) in 2016 was used to identify grass (Grassland/Herbaceous in NLCD land cover classification) and pasture (Pasture/Hay in NLCD land cover classification, Homer, 2015). Forest types were identified according to the Conus Forest Group dataset downloaded from USDA Forest Service (https://data.fs.usda.gov/geodata/rastergateway/forest_type/). This dataset is created by the USFS Forest Inventory and Analysis program and the Remote Sensing Application Center. Third, the start of the growing season (SOS) of the four vegetation types was examined based on the Normalized Difference Phenology Index (Wang et al., 2017, Text S2). Finally, variabilities of f^{esc} and Φ_F can help explain the variabilities of $SIF_{yield\ apparent.}$ We examined the differences of f^{esc} and Φ_F between croplands and non-croplands, and between corn and soybean. We also explored the spatial and temporal patterns of f^{esc} and Φ_F. The same analysis as for $SIF_{yield\ apparent}$ was conducted.

3. Results

3.1 Difference of $SIF_{yield\ apparent}$ between croplands and non-croplands

The relationship between OCO-2 $SIF_{yield\ apparent}$ and cropland fraction in different growing months from 2015 to 2018 (Fig. 3) showed a clear seasonal pattern. In May, $SIF_{yield\ apparent}$ decreased with the cropland fraction, implying that $SIF_{yield\ apparent}$ of croplands was lower than non-croplands in the early growing season. In July and August, $SIF_{yield\ apparent}$ showed an increasing trend with the increase of the cropland fraction (all statistically significant with $P<0.001$). These results indicated that during the peak growing season, cropland $SIF_{yield\ apparent}$ was higher than non-cropland $SIF_{yield\ apparent}$.

Since we have SIF footprint observations from TROPOMI in 2018, we applied the same analysis as above (Fig. S1). Generally, the results from TROPOMI observations were similar to those from OCO-2 observations, despite the different magnitudes of the slopes between $SIF_{yield\ apparent}$ and the cropland fraction. We further conducted the same analysis for SIF_{inst} (instantaneous SIF) and SIF_{par} (SIF normalized by PAR, Fig. S2). The difference between croplands and non-croplands in SIF_{inst} and SIF_{par} showed a similar seasonal pattern to that of $SIF_{yield\ apparent}$.

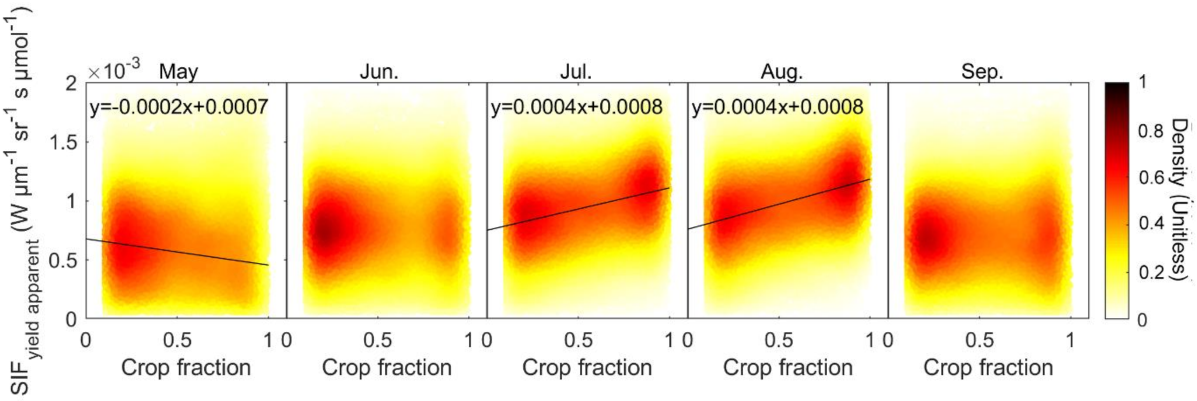

Fig. 3 Relationship between $SIF_{yield\ apparent}$ calculated from OCO-2 SIF and the fraction of croplands (corn and soybean). The linear fits and the equations are shown when the regression is significant ($p<0.001$). Only footprints with a cropland fraction larger than 10% are included.

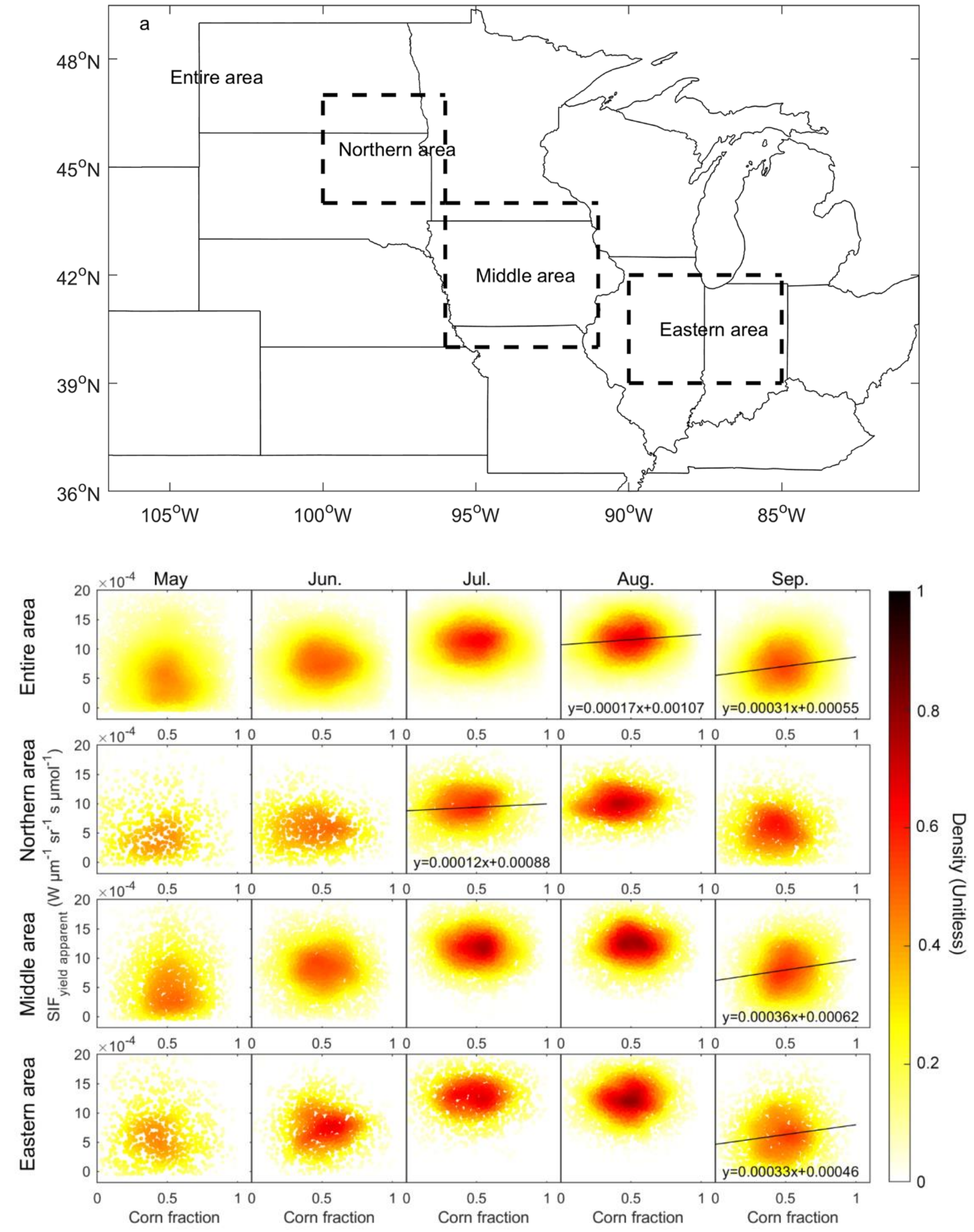

Fig. 4 Relationship between $SIF_{yield\ apparent}$ and the fraction of the OCO-2 footprint covered by corn. The upper panel illustrates the three regions that are labeled in the bottom panel. The linear fits and the equations in the bottom panel are shown only when the regression is significant ($p<0.001$). Only footprints with a cropland fraction larger than 80% were included.

3.2 Difference of $\mathrm{SIF}_{\text{yield apparent}}$ between Corn (C4) and Soybean (C3)

The relationship between OCO-2 $\mathrm{SIF}_{\text{yield apparent}}$ and corn fraction for the cropland-dominated footprints during different growing season months from 2015 to 2018 for different regions (Fig. 4) generally showed a weak linear relationship between $\mathrm{SIF}_{\text{yield apparent}}$ and corn fraction, implying that $\mathrm{SIF}_{\text{yield apparent}}$ of corn was similar to that of soybean. For the entire study domain, the relationship between $\mathrm{SIF}_{\text{yield apparent}}$ and corn fraction was positively significant ($P<0.001$) in August and September but was not significant in the other three months. We also performed a linear regression between $\mathrm{SIF}_{\text{yield apparent}}$ and corn fraction in three sub-regions (northern area, middle area, and eastern area) and in five growing season months respectively, with a total of 15 cases (Fig. 4). The relationship was significant ($P<0.001$) only in three out of the 15 cases: the northern area in July, the middle area in September, and the eastern area in September. Compared with $\mathrm{SIF}_{\text{yield apparent}}$, the difference of $\mathrm{SIF}_{\text{inst}}$ and $\mathrm{SIF}_{\text{par}}$ between corn and soybean appeared to be similar (Fig. S3-S4). $\mathrm{SIF}_{\text{inst}}$ and $\mathrm{SIF}_{\text{par}}$ of corn were significantly larger than soybean from June to September for the entire area. However, this difference was weak when the analysis was restricted to a small sub-region, with the exception of $\mathrm{SIF}_{\text{inst}}$ in the northern area.

3.3 Spatial and temporal patterns of $\mathrm{SIF}_{\text{yield apparent}}$

3.3.1 Spatial pattern and potential drivers of $\mathrm{SIF}_{\text{yield apparent}}$

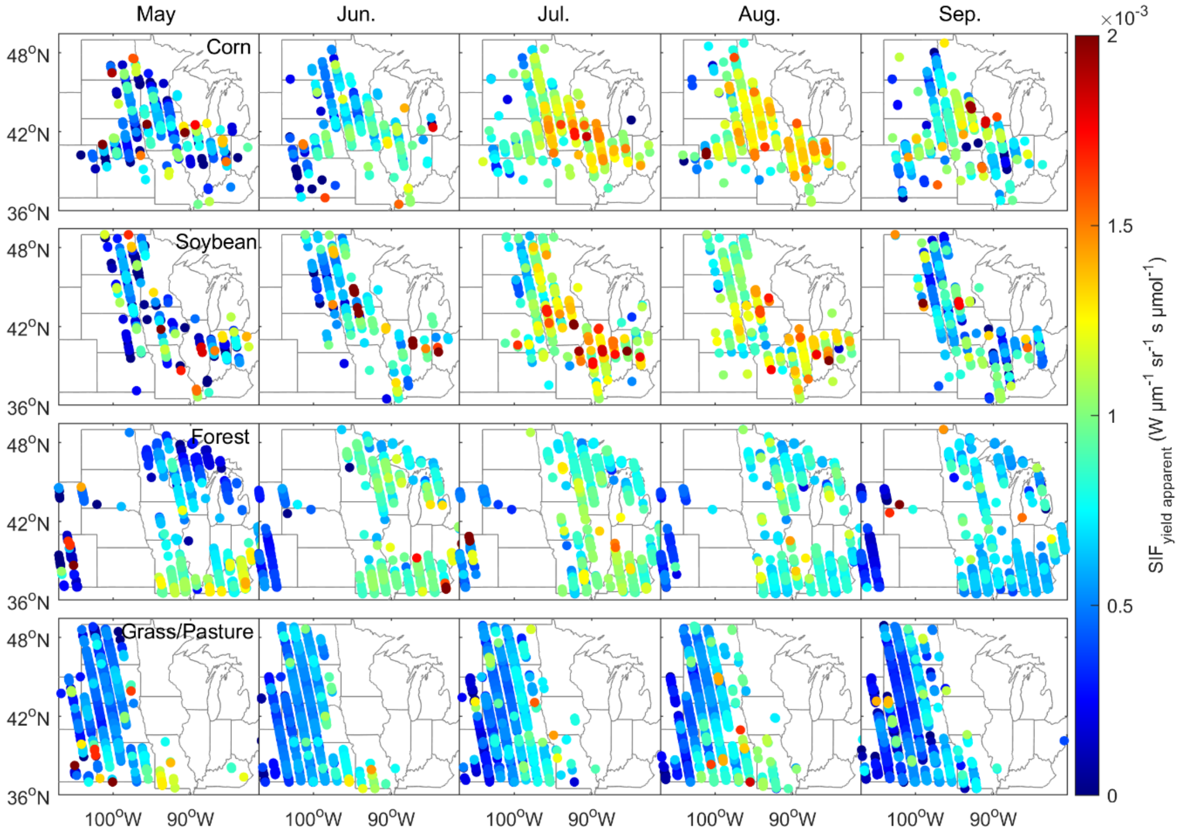

Fig. 5 Spatial distributions of SIF$_{\text{yield apparent}}$ of corn, soybean, forest, and grassland calculated from the OCO-2 data. The average of all the available SIF$_{\text{yield apparent}}$ values within a 0.5°×0.5° grid was assigned to all the footprints within the grid.

SIF$_{\text{yield apparent}}$ of corn and soybean calculated from the OCO-2 footprint data showed clear spatial patterns (Fig. 5). In May and June, the spatial difference of SIF$_{\text{yield apparent}}$ was low for both corn and soybean because it is the beginning of the growing season for those crops (Fig. S5). From July to August, SIF$_{\text{yield apparent}}$ of corn in the central Corn Belt (Iowa, Illinois, and Indiana) was higher than SIF$_{\text{yield apparent}}$ of corn in the northern and the western parts of the Corn Belt. SIF$_{\text{yield apparent}}$ of soybean showed a similar pattern to corn, despite there were fewer available observations defined as the fraction of soybean >80% of the footprint in the west.

This spatial pattern of SIF$_{\text{yield apparent}}$ for both corn and soybean can be partly explained by precipitation (Fig. 6). During the peak growing season, SIF$_{\text{yield apparent}}$ was, in general, higher in areas with higher precipitation. $SIF_{yield\ apparent}$ in July was significantly ($P<0.01$) correlated with precipitation when the temperature was fixed to a small range. The response of $SIF_{yield\ apparent}$ to temperature was not clear. The linear correlation between $SIF_{yield\ apparent}$ in July and temperature was not significant when precipitation was fixed to a small range. In September, except for a small region in the central Corn Belt with high values of $SIF_{yield\ apparent}$ of corn, $SIF_{yield\ apparent}$ of the two crop types started to decrease, possibly because both crops matured.

Spatial patterns of $SIF_{yield\ apparent}$ of forest and grass/pasture differed from those of corn and soybean (Fig. 5). In general, Forest $SIF_{yield\ apparent}$ in the west was much lower than in other regions during the growing season. Forest $SIF_{yield\ apparent}$ in the northeast and southeast were comparable. Two factors could potentially account for the observed spatial patterns. First, high $SIF_{yield\ apparent}$ was associated with high temperature and precipitation (Fig. 6). Second, the spatial distribution of the forest types and the differences of $SIF_{yield\ apparent}$ among these types could explained the spatial pattern of $SIF_{yield\ apparent}$. Among all forest types, $SIF_{yield\ apparent}$ of the dominant forest type in the west (Ponderosa Pine) was the lowest, and $SIF_{yield\ apparent}$ of the dominant forest type in the southeast (Oak/Hickory) was the highest (Fig. 7). In addition to the general spatial pattern, a decreasing pattern of $SIF_{yield\ apparent}$ from the southeast to the northeast was observed in May. A potential explanation for this observation is that the SOS of forest in the northeast was in early May or late April, whereas the SOS of forest in the southeast was in March or April (Fig. S5).

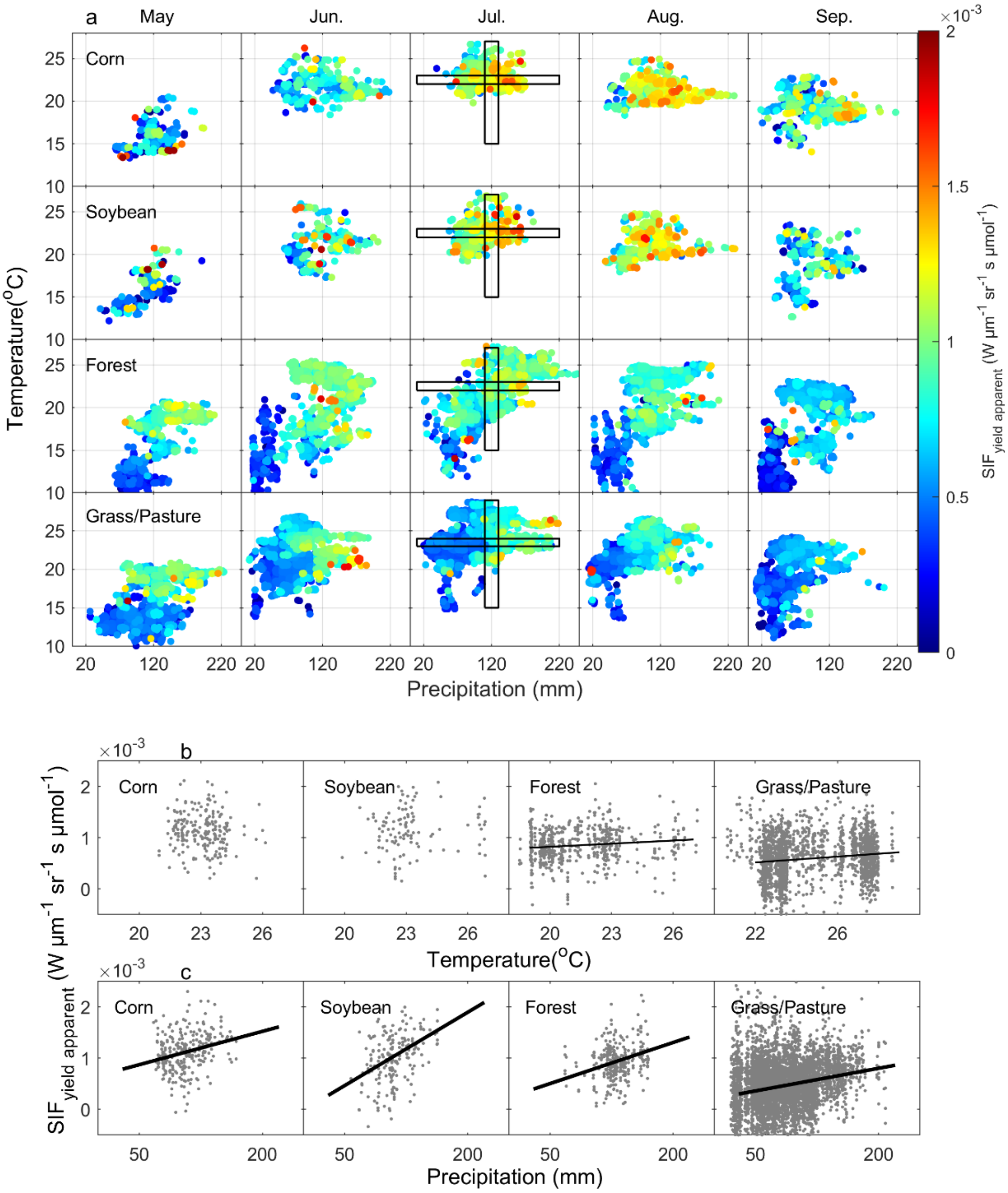

Fig. 6 a, Distributions of $\text{SIF}_{\text{yield apparent}}$ of corn, soybean, forest, and grass/pasture within a 2-D space jointly determined by monthly mean temperature (℃) and precipitation (mm). The $\text{SIF}_{\text{yield apparent}}$ was calculated from the OCO-2 footprint data from 2015 to 2018. The meteorological variables are multi-year mean values. $\text{SIF}_{\text{yield apparent}}$ was smoothed by averaging $\text{SIF}_{\text{yield}}$ within a 10 mm×0.5 ℃ window. b, Scatter plots of $\text{SIF}_{\text{yield apparent}}$ versus mean temperature used data in the vertical box shown in a. c, Scatter plots of $\text{SIF}_{\text{yield apparent}}$ versus total precipitation used data in the horizontal box shown in a. The linear fits are shown only when the regression is significant ($p<0.01$).

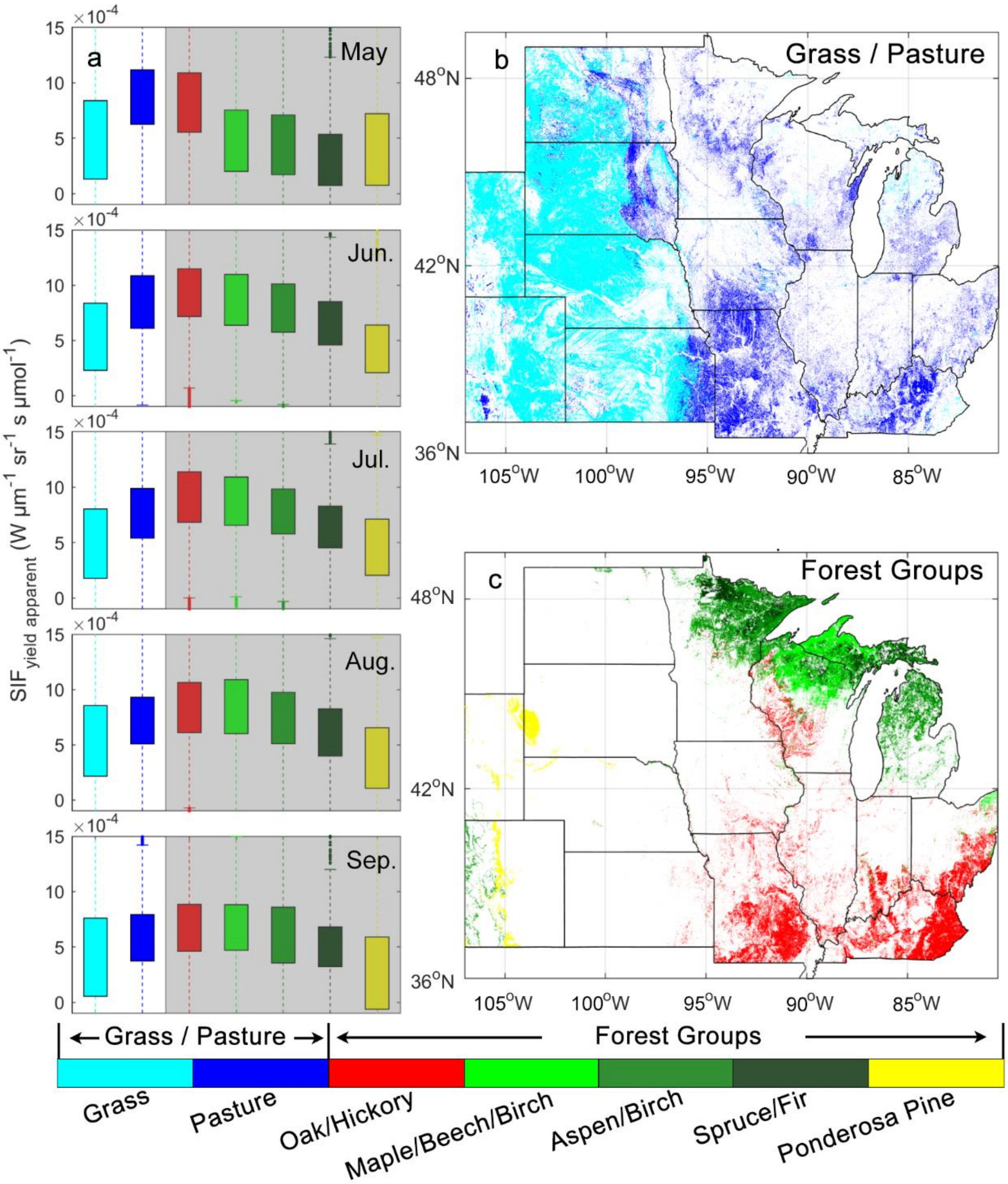

Fig. 7 Boxplots of SIF$_{\text{yield apparent}}$ of grass, pasture and different forest types for different months. Shaded areas are forest types. SIF$_{\text{yield apparent}}$ was calculated from OCO-2 footprint data from 2015 to 2018.

The spatial pattern of SIF$_{\text{yield apparent}}$ in grass/pasture demonstrated a clear gradient of increase from west to east. This pattern was consistent across different growing months.

Grass/pasture is mainly distributed in the western part of the U.S. Midwest. $\mathrm{SIF}_{\mathrm{yield\ apparent}}$ of grass/pasture appeared to be lower than other vegetation types, which may also contribute to a lower spatial variability. Similar to the forest, the spatial variability could potentially be explained by two factors. First, $\mathrm{SIF}_{\mathrm{yield\ apparent}}$ of pasture was higher than that of grassland while pasture was mainly distributed in the east and grassland was distributed in the west. However, this may only account for a small portion of the spatial pattern of $\mathrm{SIF}_{\mathrm{yield\ apparent},}$ because the number of footprints in pasture areas was limited. Second, high $\mathrm{SIF}_{\mathrm{yield\ apparent}}$ was observed in the wet-warm region (Fig. 6), implying the impact of meteorological factors on $\mathrm{SIF}_{\mathrm{yield\ apparent.}}$ $\mathrm{SIF}_{\mathrm{yield\ apparent}}$ in July was positively correlated with temperature (or precipitation) after fixing precipitation (or temperature, Fig. 6).

To further corroborate our findings, we examined the spatial pattern of $\mathrm{SIF}_{\mathrm{yield\ apparent}}$ for the four vegetation types in 2018 using TROPOMI footprint data, as Fig. S6. Compared with the results from OCO-2, the spatial pattern of $\mathrm{SIF}_{\mathrm{yield\ apparent}}$ of corn from TROPOMI showed high values in eastern Nebraska, southern Iowa, and Illinois in June. For soybean, $\mathrm{SIF}_{\mathrm{yield\ apparent}}$ was high in the southern region. Despite these slight differences, results from the two datasets were similar. We also explored spatial patterns of $\mathrm{SIF}_{\mathrm{par}}$ and $\mathrm{SIF}_{\mathrm{inst}}$ and found similar spatial patterns to $\mathrm{SIF}_{\mathrm{yield\ apparent}}$ (Fig. S7-S8).

3.3.2 Temporal (Seasonal) pattern of $\mathrm{SIF}_{\mathrm{yield\ apparent}}$

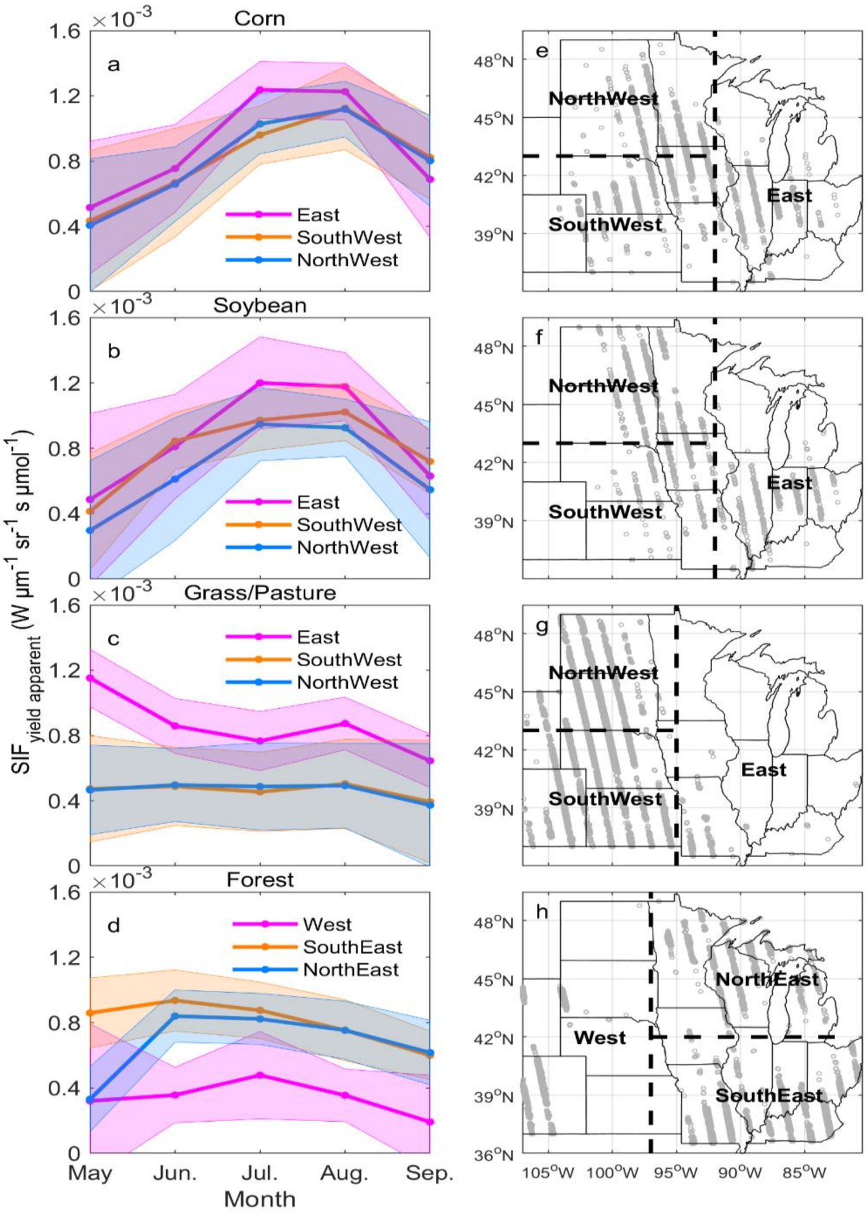

Fig. 8 Seasonal patterns of SIF$_{\text{yield apparent}}$ of corn, soybean, forest, and grassland in different regions, from OCO-2 footprint data (a-d). Each line was calculated as the median value of all footprints and all years within a specific region. Shading indicates one standard

SIF$_{\text{yield apparent}}$ of corn, soybean, grass/pasture, and forest had different temporal variabilities from May to September (Fig. 8). Seasonal patterns of SIF$_{\text{yield apparent}}$ of corn and soybean showed a 'bell' shape. SIF$_{\text{yield apparent}}$ of corn and soybean increased from May onward, reaching the highest values in July or August, before decreasing to a lower value in September when crops began to senesce. Despite differences in the magnitude of $\mathrm{SIF}_{\mathrm{yield\ apparent}}$, this seasonal pattern was consistent across different sub-regions.

For grass/pasture, the seasonal pattern of $\mathrm{SIF}_{\mathrm{yield\ apparent}}$ in the west was remarkably different from that in the east (Fig. 8). $\mathrm{SIF}_{\mathrm{yield\ apparent}}$ in the west showed a slightly decreasing trend from May to September, while in the east, $\mathrm{SIF}_{\mathrm{yield\ apparent}}$ decreased from May to September with a higher magnitude of $\mathrm{SIF}_{\mathrm{yield\ apparent}}$ during the growing season. Notably, there was a rapid decrease in $\mathrm{SIF}_{\mathrm{yield\ apparent}}$ from May to June. This may indicate that the seasonal pattern of $\mathrm{SIF}_{\mathrm{yield\ apparent}}$ of grass, which dominates in the west, differs from that of pasture, which dominates in the east (Fig. 7).

For forest distributed in different sub-regions, there was a lack of a universal temporal pattern, possibly due to the different dominant forest types in these sub-regions (Fig. 7). In the west, $\mathrm{SIF}_{\mathrm{yield\ apparent}}$ of forest started increasing in May, peaked in July and then decreased until September. In the southeast, $\mathrm{SIF}_{\mathrm{yield\ apparent}}$ showed a decreasing trend from May to September. In the northeast, $\mathrm{SIF}_{\mathrm{yield\ apparent}}$ of the forest showed a very large increase from May to June. possibly because the growing season of the forests in this area starts in May after which time $\mathrm{SIF}_{\mathrm{yield\ apparent}}$ decreases until September.

We further examined seasonal patterns of $\mathrm{SIF}_{\mathrm{yield\ apparent}}$ derived from TROPOMI in 2018 (Fig S9.). As expected, the monthly dynamics of $\mathrm{SIF}_{\mathrm{yield\ apparent}}$ from May to September derived from the two satellite observations were similar, except for grass/pasture in the east where $\mathrm{SIF}_{\mathrm{yield\ apparent}}$ from TROPOMI did not show a clear decreasing trend from May to September as OCO-2. In addition, the seasonal patterns of $\mathrm{SIF}_{\mathrm{par}}$ and $\mathrm{SIF}_{\mathrm{inst}}$ were similar to those of $\mathrm{SIF}_{\mathrm{yield\ apparent}}$ (Fig. S10-S11).

3.4 Variability of f^{esc} and Φ_F

The density plots showing the relationships between Φ_F or f^{esc} and croplands fraction (Fig. S12) suggested that both Φ_F and f^{esc} contributed to the observed difference of $SIF_{yield\ apparent}$ between croplands and non-croplands. f^{esc} had a strong linear relationship with crop fraction during different growing months, while the relationship between Φ_F and crop fraction was relatively weak compared with the relationship between f^{esc} and crop fraction. The seasonal dynamics of the slope between f^{esc} and crop fraction were similar to those observed between $SIF_{yield\ apparent}$ and crop fraction. These results imply that f^{esc} may dominate the observed differences in $SIF_{yield\ apparent}$ between croplands and non-croplands.

Differences of Φ_F or f^{esc} between corn and soybean can be detected during some months (Fig. S13-S14), although $SIF_{yield\ apparent}$ of corn and soybean were not significantly different across the three sub-regions (Fig 5). For example, in August, the Φ_F of corn was larger than that of soybean, while the f^{esc} of corn was smaller than that of soybean in the three sub-regions or over the whole study domain. In September, corn f^{esc} was significantly lower than soybean f^{esc} while the Φ_F of corn was larger than that of soybean in the east and middle sub-regions or over the whole domain.

Fig. S15 and Fig S16 showed spatial patterns of f^{esc} and Φ_F. The spatial pattern of f^{esc} was similar to that of $SIF_{yield\ apparent}$. On the other hand, the spatial pattern of Φ_F contained more noise. No clear spatial pattern was found except that Φ_F of grass/pasture increased from the west to the east, which matched with the pattern of $SIF_{yield\ apparent}$. Fig. 9 showed the seasonal patterns of Φ_F and f^{esc}. Φ_F generally remained stable during the growing season for all the four vegetation

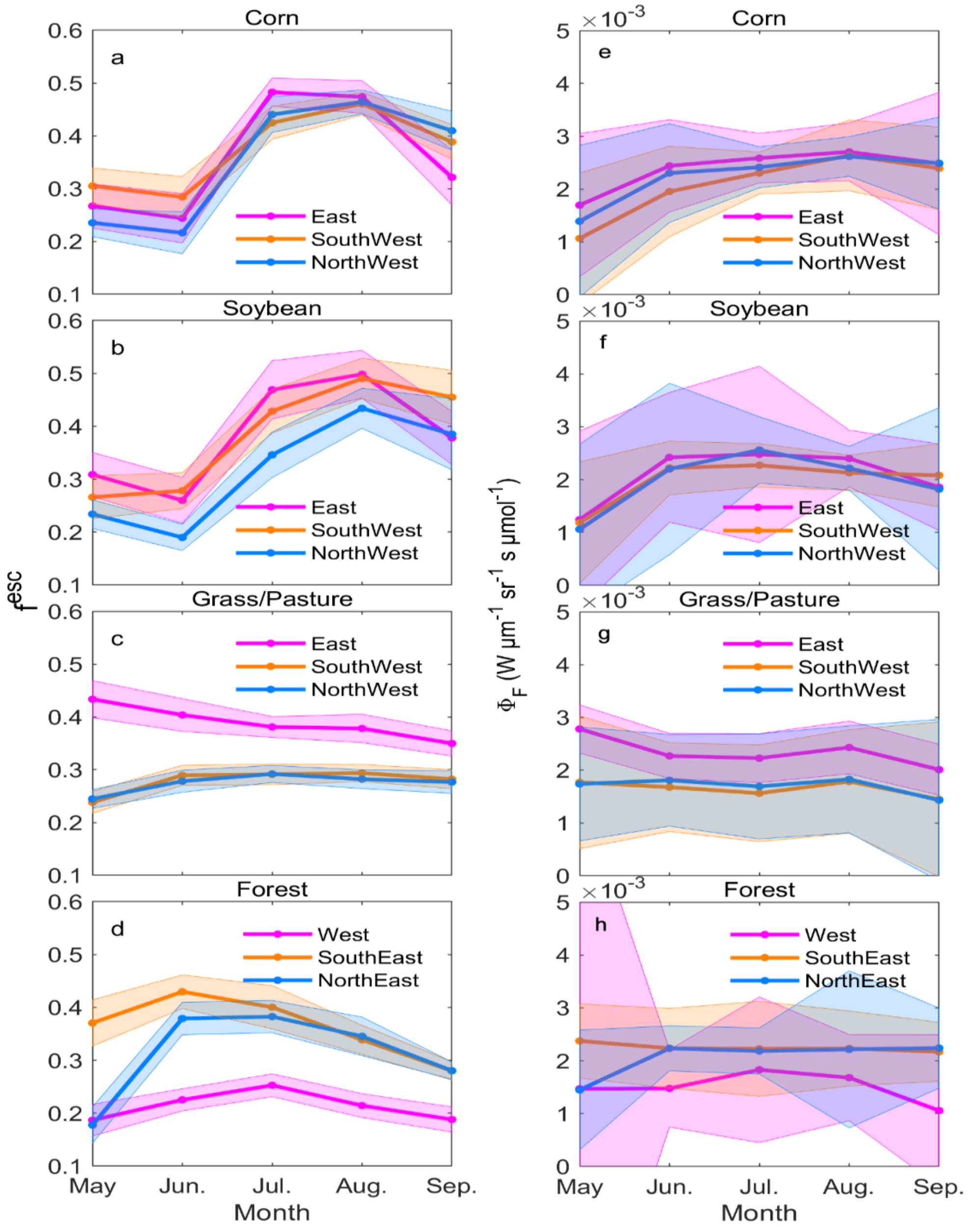

Fig. 9 Seasonal patterns of Φ_F and f^{esc} of corn, soybean, forest, and grassland in different regions from OCO-2 footprint data. Each line was calculated as the median value of all

types except for the increase from May to June for croplands. Conversely, f^{esc} showed a strong seasonal variability which was similar to that of $SIF_{yield\ apparent}$.

4. Discussion

4.1 Variability of $\mathrm{SIF}_{\mathrm{yield\ apparent}}$

Our study shows that $\mathrm{SIF}_{\mathrm{yield\ apparent}}$ of croplands is significantly larger than non-croplands during the peak growing season in the U.S. Midwest (July-August). This result is consistent with the spatial pattern of SIF during the same period in the U.S. Midwest observed in previous research which reveals much higher SIF values in the Corn Belt than in the surrounding regions (Guanter et al., 2014; Gentine and Alemohammad 2018; Joiner et al., 2013). The higher SIF of croplands compared with non-croplands is also supported by the OCO-2 footprint SIF data used in this study (Fig. S3). Our analysis of $\mathrm{SIF}_{\mathrm{yield\ apparent}}$ demonstrates that the differences in $\mathrm{SIF}_{\mathrm{yield\ apparent}}$ between croplands and non-croplands could partly contribute to the remarkably high SIF of the U.S. Corn Belt. APAR also contributes to the high SIF (Fig. S17) but is less important than $\mathrm{SIF}_{\mathrm{yield\ apparent}}$. Because the ratio of croplands $\mathrm{SIF}_{\mathrm{yield\ apparent}}$ to non-croplands $\mathrm{SIF}_{\mathrm{yield\ apparent}}$ in peak season, which can be roughly estimated from equations in Fig. 3 when crop fraction is set as 1 and 0, is much higher than that of APAR (Fig. S17).

The difference in $\mathrm{SIF}_{\mathrm{yield\ apparent}}$ between the C4 (corn) and C3 (soybean) crops is small (Fig. 4). In August and September, the Φ_F of corn is larger than soybean, while the f^{esc} of corn shows the opposite patterns which potentially explain the similar $\mathrm{SIF}_{\mathrm{yield\ apparent}}$ of corn and soybean in the two months (Fig. S13 and S14). For some other months, the similarities in f^{esc} could possibly explain the similar patterns in $\mathrm{SIF}_{\mathrm{yield\ apparent}}$ given the small variation and differences in Φ_F. Wood et al., (2017) examined OCO-2 footprint SIF retrievals in Iowa and southern Minnesota and found a similar magnitude of fluorescence (F_s, SIF normalized by the cosine of the solar zenith angle) from corn and soybean canopies. It is noteworthy that we also do not find any significant difference in $\mathrm{SIF}_{\mathrm{par}}$ (SIF normalized by PAR) between corn and soybean in a similar region (middle area in Fig. 5). Here $\mathrm{SIF}_{\mathrm{par}}$ is a similar concept to F_{s} because the cosine of the solar zenith angle is a good proxy of PAR. However, when we focus on the whole Midwest region, both $\mathrm{SIF}_{\mathrm{inst}}$ and $\mathrm{SIF}_{\mathrm{par}}$ of corn are larger than the counterparts of soybean during the peak season probably because of the different spatial distribution between corn and soybean.

We present different spatial patterns of $\mathrm{SIF}_{\mathrm{yield\ apparent}}$ of different vegetation types using satellite footprint data. Previous studies have investigated spatial patterns of $\mathrm{SIF}_{\mathrm{yield\ apparent}}$ at regional or global scales (Joiner et al., 2011; Li et al., 2018b; Song et al., 2018) using coarse-spatial-resolution SIF products. Our study confirms that meteorological variables (e.g. precipitation and temperature) play roles in determining $\mathrm{SIF}_{\mathrm{yield\ apparent}}$ within certain vegetation types. In general, more precipitation leads to higher $\mathrm{SIF}_{\mathrm{yield\ apparent}}$ for all the vegetation types, while the correlation between temperature and $\mathrm{SIF}_{\mathrm{yield\ apparent}}$ is weak. Considering that some croplands are irrigated and precipitation might not directly affect the observed SIF, we checked the impact of VPD (Fig. S18) on $\mathrm{SIF}_{\mathrm{yield\ apparent}}$ and found negative correlations between VPD and $\mathrm{SIF}_{\mathrm{yield\ apparent}}$ for most cases.

The seasonal patterns of corn and soybean $\mathrm{SIF}_{\mathrm{yield\ apparent}}$ from May to September generally follow the growth cycle of crops in the U.S. Midwest. The ‘bell’ shape curve was also found for wheat in northwest India and crops in western Russia during the growing season, based on the GOME-2 gridded dataset (Song et al., 2018; Yoshida et al., 2015). However, we did not observe this bell shape of $\mathrm{SIF}_{\mathrm{yield\ apparent}}$ for forest and grass/pasture ecosystems, which is a departure from prior studies (Yoshida et al., 2015). By extending the growing season to include

April and October, we found that $\mathrm{SIF}_{\mathrm{yield\ apparent}}$ of forest and grass/pasture increased during the start of the growing season except for grass in the west and decreased during the end of the growing season, although the amplitude of the shift of $\mathrm{SIF}_{\mathrm{yield\ apparent}}$ was not large (Fig. S19). To confirm the results from satellite data, we also checked the seasonal pattern of $\mathrm{SIF}_{\mathrm{yield\ apparent}}$ using ground observations at two sites at Nebraska (Text S3). Fig. S20 showed that there was a decreasing trend of $\mathrm{SIF}_{\mathrm{yield\ apparent}}$ from peak season to September for corn in 2017 and soybean in 2018 which is consistent with the satellite observation. Currently, we cannot provide a more detailed comparison because the ground data only cover the second half of the growing season and there are not enough OCO-2 footprints that cover the field sites. The factors that we observed to correlate with the spatial pattern of $\mathrm{SIF}_{\mathrm{yield\ apparent}}$, such as precipitation and temperature, may influence the seasonal cycle of $\mathrm{SIF}_{\mathrm{yield\ apparent}}$ (Li et al., 2018b). We also recognize that the seasonal cycle of plant growth usually resembles the seasonal cycle of environmental factors, which makes it difficult to fully disentangle the influences of abiotic factors (environmental factors) and physical factors (e.g. canopy structure, leaf optical property) on $\mathrm{SIF}_{\mathrm{yield\ apparent}}$.

4.2 Variabilities of f^{esc} and Φ_F

The apparent canopy SIF yield is a product of f^{esc} and Φ_F. Our results suggest that f^{esc} may be a major driver of the observed seasonal dynamic of $\mathrm{SIF}_{\mathrm{yield\ apparent}}$. The seasonal pattern of f^{esc} is similar to that of $\mathrm{SIF}_{\mathrm{yield\ apparent}}$ for all the four vegetation types. We also notice that some results are not as expected. For example, the seasonal pattern of f^{esc} of crops shows a large increase from June to July. At first sight, we might expect that f^{esc} should decrease with the rapid increase of LAI during the early growing season because the fraction of canopy gaps for SIF to escape will decrease. However, for far-red SIF, previous studies based on the Soil Canopy Observation, Photochemistry and Energy (SCOPE) model reported a contrary result (Fournier et al., 2012; Du et al., 2017; Yang and Van der Tol, 2018). Escaping ratio increases with LAI due to multiple scattering. LAD can also influence f^{esc}. Some simulation analyses show that escaping ratio with planophile or spherical LAD is much higher than that of erectophile vegetation (Migliavacca et al., 2017; Zeng et al., 2019), and experimental data also support this argument (Du et al., 2017). However, more field observations are needed to address whether there is a shift of erectophile canopy to planophile canopy for crops during the early season. Another possible cause of the observed pattern is the increasing canopy cover in spring in driving the increasing f^{esc} estimation. LAI and LAD could also be used to explain the low value of f^{esc} of grassland in the west because the grass in arid and semi-arid regions usually has low LAI and erectophile LAD (Diana et al., 2000; Holder et al., 2012). Compared to f^{esc}, the monthly median value of Φ_F remains stable. However, the high variance of Φ_F within a month implies that Φ_F may play an important role at small time scales. With regard to the spatial pattern, we find a clear spatial pattern of f^{esc}, while the spatial pattern of Φ_F has more noise. A probable explanation is that f^{esc} is determined by the canopy structure and leaf optical properties, which are stable during specific time periods, whereas Φ_F reflects the physiology of vegetation which can be influenced by more rapidly varying environmental conditions. Another simple explanation is that the estimation of SIF contains more noise than the estimation of f^{esc}.

The impact of meteorological factors on $SIF_{yield\ apparent}$ could be attributable at least in part to both f^{esc} and Φ_F. The spatial pattern of f^{esc} can be influenced by meteorological factors.

For example, the LAD of soybeans is controlled by leaf water potential, and under water stress conditions, soybean leaves tend to be more vertical (Oosterhuis et al., 1985). Additionally, plants in arid areas may have steeper leaf angles to reduce rainfall interception by leaves and increase soil infiltration (Holder, 2012) or to minimize light interception and leaf temperature which is usually in excess in those regions. Similarly, LAI of grass has been reported to increase with precipitation (Diana et al., 2000), which could also change f^{esc}. Φ_F reflects the distribution of the absorbed energy, which is likely also sensitive to meteorological conditions through the dynamics changes of non-photochemical quenching (NPQ) and photochemical quenching (PQ) in relation to various plant abiotic stresses (Cendrero-mateo et al., 2015; Frankenberg and Berry, 2018; Xu et al., 2018).

4.3 Uncertainties and Limitations

Quantifying f^{esc} and Φ_F over large scales is a challenging but important task. A handful of methods have been developed (Liu et al., 2018; Romero et al., 2018; Yang and van der Tol, 2018; Zeng et al., 2019). We adopt a method developed recently by Zeng et al. (2019), which can be easily applied over large spatial scales. The approach is demonstrated to be effective by simulation analysis using the SCOPE model and the Discrete Anisotropic Radiative Transfer (DART) model. But some uncertainties are introduced during the application of the approach. First, wavelengths of SIF (771nm and 757 nm for OCO-2, 740 nm for TROPOMI) are not consistent with the MODIS NIR band (858 nm) which is used to calculate f^{esc}. However, this impact is small in practice, as assessed by Zeng et al., (2019). Second, the sun-canopy-sensor geometry of SIF is different from that of MODIS. To minimize this effect, we only used OCO-2 observations taken in ‘nadir’ mode, TROPOMI data with view zenith angle less than 10 degrees, and MODIS Nadir BRDF-Adjusted Reflectance data. The uncertainty caused by sun-canopy-sensor geometry could also influence the seasonal pattern of $\mathrm{SIF}_{\mathrm{yield\ apparent}}$ due to the varying solar zenith angle for different seasons. Third, when vegetation cover is extremely low, this approach can break down (Zeng et al., 2019). Although there are some potential uncertainties in the analysis, it is an important step toward decomposing $\mathrm{SIF}_{\mathrm{yield\ apparent}}$ into f^{esc} and Φ_F, which represents a necessary advancement toward fully interpreting observed SIF signals.

Accurate estimation of $\mathrm{SIF}_{\mathrm{yield\ apparent}}$ depends on reliable fPAR datasets. There are several fPAR products available. These datasets are produced from measurements from different instruments using different retrieval algorithms which potentially generate discrepancies among fPAR datasets. For example, inter-comparisons with other fPAR products show that there is an overestimation of the retrievals at low fPAR values in MODIS fPAR products (Yan et al., 2016). In this study, we used four approaches to estimate fPAR. Fig. S21 showed the standard deviation (SD) of $\mathrm{SIF}_{\mathrm{yield\ apparent}}$ calculated from the four fPAR values. The results demonstrated that the SD was much lower than the corresponding mean $\mathrm{SIF}_{\mathrm{yield\ apparent}}$ (Fig. 5) for most cases, while for corn and soybean in May, the SD could be higher. This is probably because the relative uncertainties of all terms in $\mathrm{SIF}_{\mathrm{yield\ apparent}}$ and f^{esc} are higher for low fPAR values.

Although this study used state-of-the-art satellite-based SIF products, these SIF products still have limitations. First, SIF is a weak signal consisting of 1%-5% of the total absorbed energy (Frankenberg et al., 2018), and satellite-based SIF measurements still contain possibly uncertainties. Sun et al., (2017) compared OCO-2 retrievals with airborne measurements of SIF with the Chlorophyll Fluorescence Imaging Spectrometer (CFIS) and found R^2 between OCO-2 and CFIS SIF was 0.71. Second, OCO-2 footprint observations are discrete samples, and they are not spatially and temporally continuous. We also used TROPOMI footprint data which provides better spatial and temporal details due to the greatly improved spatio-temporal coverage of the dataset compared with OCO-2. However, we found some areas with lower valid data coverage, for example, soybean crops in Iowa. This is probably because the spatial resolution of TROPOMI is not fine enough to get enough pure footprints. The readers should be aware that there is a consistent difference in the absolute value of SIF between OCO-2 and TROPOMI because the wavelength of the two SIF retrievals is not the same. An alternative method would be to use downscaled (Duveiller and Cescatti, 2016) or reconstructed (Gentine and Alemohammad, 2018; Li and Xiao, 2019; Y. Zhang et al., 2018) gridded SIF data. However, we purposely decided not to use any of these SIF products here, as these downscaled or reconstructed data include assumptions that could skew our findings. Third, the temporal frequency (monthly) in our analysis offers only a coarse view of seasonal patterns. Especially during the period from May to June for crops and forests in the northeast when the plants start to grow and the canopy structures and physiology status change rapidly. This could potentially be solved with TROPOMI data with high temporal frequency in the future. New measurements from the site level scale could provide more information. Finally, $SIF_{yield\ apparent}$ should be wavelength dependent since both the emitted SIF spectrum and the reflectance at leaf level are wavelength-dependent (Verrelst et al., 2015). However, the OCO-2 footprint dataset provides SIF at 771 nm and 757 nm, while TROPOMI SIF is only available at 740 nm.

4.4 Contribution to understand SIF and the $SIF_{yield\ apparent}$: LUE relationship

This study's findings have many important implications. Most importantly, APAR and $SIF_{yield\ apparent}$ jointly determine variability in SIF. APAR correlates more with plant structural properties and pigment content, while $SIF_{yield\ apparent}$ is likely to carry both canopy structure and plant physiology signals. Leaf-level and canopy-level studies have found evidence of potential effects from plant physiological such as Vcmax etc. (Zhang et al., 2014), stomatal conductance (Flexas et al., 2002), and electron transport rate (Guan et al., 2016), as well as canopy structure (Fournier et al., 2012) such as LAD (Du et al., 2017; Zhang et al., 2016) and LAI (Du et al., 2017; Yang and van der Tol, 2018). Our regional-level study reveals differences in $SIF_{yield\ apparent}$ across space and time and between vegetation cover types implying the importance of $SIF_{yield\ apparent}$ in driving the variability of canopy SIF. The findings further emphasize the important role of the escaping ratio (canopy structure).

The significant variations of $SIF_{yield\ apparent}$ revealed in this study may help foster modeling of GPP at large scales. Similarities between the GPP and SIF equations (Equation 1 and 2) lead to a formal equivalence between GPP: SIF and LUE: $SIF_{yield\ apparent}$. The equivalence of the two equations could help to estimate GPP directly from satellite SIF observation and to better understand what determines the GPP: SIF slope but only when a mechanistic relationship between LUE and $SIF_{yield\ apparent}$ is established. Physiologically, there is a complicated coupling between LUE and Φ_F under various light and plant stress conditions (Schlau-Cohen and Berry 2015, Van Der Tol et al., 2014). In addition to Φ_F, f^{esc} and LUE may also casually covary due to temporal covariation between plant structure and plant function. The near-infrared reflectance is related to leaf nitrogen content and the ratio of sun-exposed leaf area to total leaf area which are determinants of photosynthetic capacity (Ollinger et al., 2008, Knyazikhin et al., 2013). Meanwhile, the near-infrared reflectance is also supposed to be correlated to f^{esc} (Yang and van der Tol, 2018). Thus the variability of f^{esc} may be associated with the variability of LUE. Studies using field-level observations have intended to provide an empirical estimation of the LUE: $SIF_{yield\ apparent}$ relationship (Damm et al., 2010; Miao et al., 2018; Verma et al., 2017; Yang et al., 2018; Yang et al., 2015). However, the relationship varies across different seasons and environmental conditions. Further efforts are required by combining field-level observations, especially long-term observations (Miao et al., 2018; Yang et al., 2018), and satellite observations to constrain these relationships and advance understanding of the underlying controlling factors.

5. Conclusions

In this study, we conducted a systematic assessment of the spatio-temporal variability of $SIF_{yield\ apparent}$ of corn, soybean, forest, and grass/pasture in the U.S. Midwest during the crop growing season. The state-of-the-art satellite-based SIF products from OCO-2 and TROPOMI footprint retrievals were used to estimate $SIF_{yield\ apparent}$ of specific vegetation types. The high spatial resolution of the footprints enables accurate estimation of $SIF_{yield\ apparent}$ for each vegetation type by reducing the intra-pixel mixture effects. Our analysis leads to four main conclusions: 1) $SIF_{yield\ apparent}$ of croplands (i.e. corn and soybean) was higher than that of non-croplands during the peak growing season (July and August) which contributed to the high SIF observed in the U.S. Corn Belt in the summer. 2) $SIF_{yield\ apparent}$ of corn and soybean did not show significant differences. 3) Different seasonal and spatial patterns of $SIF_{yield\ apparent}$ were observed among the four vegetation types, which can be partially explained by meteorological factors (i.e. precipitation and temperature) and intra-vegetation type variability (i.e. among different forest types, and between grass and pasture). 4) The escaping ratio may be the major driver of the observed variability of $\text{SIF}_{\text{yield apparent}}$.

Acknowledgments:

K.G., C.W., J.C., B.P., C.A., G.M., thank the financial support from NASA Terrestrial Ecosystem Program through the Carbon Monitoring System Program (80NSSC18K0170) and NASA New Investigator Program (NNX16AI56G), and USDA NIFA Program. K.G. and C.F. have been supported by the NASA Terrestrial Ecosystem Program through the Carbon Cycle Science Program (NNX17AE14G).

References:

Baret, F., Weiss, M., Lacaze, R., Camacho, F., Makmara, H., Pacholczyk, P., Smets, B. 2013. GeoV1: LAI, FAPAR Essential Climate Variables and FCOVER global time series capitalizing over existing products. Part 1: Principles of development and production. Remote Sensing of Environment, 137, 299–309. https://doi.org/10.1016/j.rse.2012.12.027

Beer, C., Reichstein, M., Tomelleri, E., Ciais, P., Jung, M., Carvalhais, N., Rodenbeck, C., Arain, M.A., Baldocchi, D., Bonan, G.B., Bondeau, A., Cescatti, A., Lasslop, G., Lindroth, A., Lomas, M., Luyssaert, S., Margolis, H., Oleson, K.W., Roupsard, O., Veenendaal, E., Viovy, N., Williams, C., Woodward, F.I., Papale, D., 2010. Terrestrial Gross Carbon Dioxide Uptake: Global Distribution and Covariation with Climate. Science. 329, 834–838. https://doi.org/10.1126/science.1184984

Cendrero-mateo, M.P., Carmo-silva, A.E., Porcar-castell, A., Hamerlynck, E.P., Papuga, S.A., Moran, M.S., 2015. Dynamic response of plant chlorophyll fluorescence to light , water and nutrient availability. Functional Plant Biology. 42, 746-757.

https://doi.org/10.1071/FP15002

Colombo, R., Celesti, M., Bianchi, R., Campbell, P.K.E., Cogliati, S., Cook, B.D., Corp, L.A., Damm, A., Domec, J.C., Guanter, L., Julitta, T., Middleton, E.M., Noormets, A., Panigada, C., Pinto, F., Rascher, U., Rossini, M., Schickling, A., 2018. Variability of sun-induced chlorophyll fluorescence according to stand age-related processes in a managed loblolly pine forest. Glob. Chang. Biol. 24, 2980–2996. https://doi.org/10.1111/gcb.14097

Daly, C., Halbleib, M., Smith, J.I., Gibson, W.P., Doggett, M.K., Taylor, G.H., Curtis, J., and Pasteris, P.A., 2008. Physiographically-sensitive mapping of temperature and precipitation across the conterminous United States. International Journal of Climatology, 28, 2031-2064. https://doi.org/10.1002/joc.1688

Damm, A., Erler, A., Gioli, B., Hamdi, K., Hutjes, R., Kosvancova, M., et al. (2010). Remote sensing of sun induced fluorescence yield to improve modelling of diurnal courses of gross primary production (GPP). Global Change Biology, 16, 171–186. https://doi.org/10.1111/j.1365-2486.2009.01908.x

Damm, A., Guanter, L., Paul-Limoges, E., van der Tol, C., Hueni, A., Buchmann, N., Eugster, W., Ammann, C., Schaepman, M.E., 2015. Far-red sun-induced chlorophyll fluorescence shows ecosystem-specific relationships to gross primary production: An assessment based on observational and modeling approaches. Remote Sensing of Environment 166, 91-105. https://doi.org/10.1016/j.rse.2015.06.004

Diana, R., Debra, P., William, K., 2000. Changes in grassland canopy structure across a precipitation gradient. J. Veg. Sci. 11, 359–368. https://doi.org/10.2307/3236628

Du, S., Liu, L., Liu, X., Hu, J., 2017. Response of Canopy Solar-Induced Chlorophyll Fluorescence to the Absorbed Photosynthetically Active Radiation Absorbed by Chlorophyll. Remote Sens. 9, 911. https://doi.org/10.3390/rs9090911

Duveiller, G., Cescatti, A., 2016. Remote Sensing of Environment Spatially downscaling sun-induced chlorophyll fluorescence leads to an improved temporal correlation with gross primary productivity. Remote Sens. Environ. 182, 72–89. https://doi.org/10.1016/j.rse.2016.04.027

Flexas, J., Mariano Escalona, J., Evain, S., Gulías, J., Moya, I., Barry Osmond, C., Medrano, H., 2002. Steady-state chlorophyll fluorescence (fs) measurements as a tool to followvariations of net CO2 assimilation and stomatal conductance during water-stress in c3 plants. Physiologia Plantarum. 114, 231–240. https://doi.org/10.1034/j.1399-3054.2002.1140209.x

Fournier, A., Daumard, F., Champagne, S., Ounis, A., Goulas, Y., Moya, I., 2012. Effect of canopy structure on sun-induced chlorophyll fluorescence. ISPRS Journal of Photogrammetry and Remote Sensing 68, 112-120. https://doi.org/10.1016/j.isprsjprs.2012.01.003

Frankenberg, C., Berry, J., 2018. Solar Induced Chlorophyll Fluorescence: Origins, Relation to Photosynthesis and Retrieval. Comprehensive Remote Sensing. Elsevier. 1986, 143-162 https://doi.org/10.1016/B978-0-12-409548-9.10632-3

Frankenberg, C., Dell, C.O., Berry, J., Guanter, L., Joiner, J., Köhler, P., Pollock, R., Taylor, T.E., 2014. Prospects for chlorophyll fl uorescence remote sensing from the Orbiting Carbon Observatory-2. Remote Sens. Environ. 147, 1–12. https://doi.org/10.1016/j.rse.2014.02.007

Frankenberg, C., Fisher, J.B., Worden, J., Badgley, G., Saatchi, S.S., Lee, J.E., Toon, G.C., Butz, A., Jung, M., Kuze, A., Yokota, T., 2011. New global observations of the terrestrial carbon cycle from GOSAT: Patterns of plant fluorescence with gross primary productivity. Geophys. Res. Lett. 38, 1–6. https://doi.org/10.1029/2011GL048738

Gentine, P., Alemohammad, S.H., 2018. Reconstructed Solar-Induced Fluorescence: A Machine Learning Vegetation Product Based on MODIS Surface Reflectance to Reproduce GOME-2 Solar-Induced Fluorescence. Geophys. Res. Lett. 45, 3136–3146. https://doi.org/10.1002/2017GL076294

Guan, K., Berry, J.A., Zhang, Y., Joiner, J., Guanter, L., Badgley, G., Lobell, D.B., 2016. Improving the monitoring of crop productivity using spaceborne solar-induced fluorescence. Glob. Chang. Biol. 22, 716–726. https://doi.org/10.1111/gcb.13136

Guanter, L., Aben, I., Tol, P., Krijger, J.M., Hollstein, A., Köhler, P., Damm, A., Joiner, J., Frankenberg, C., 2015. Potential of the TROPOspheric Monitoring Instrument (TROPOMI) onboard the Sentinel-5 Precursor for the monitoring of terrestrial chlorophyll fluorescence. Atmos. Meas. Tech., 8, 1337–1352.

https://doi.org/10.5194/amt-8-1337-2015

Guanter, L., Frankenberg, C., Dudhia, A., Lewis, P.E., Gómez-dans, J., Kuze, A., Suto, H., Grainger, R.G., 2012. Retrieval and global assessment of terrestrial chlorophyll fl uorescence from GOSAT space measurements. Remote Sens. Environ. 121, 236–251. https://doi.org/10.1016/j.rse.2012.02.006

Guanter, L., Zhang, Y., Jung, M., Joiner, J., Voigt, M., Berry, J.A., Frankenberg, C., Huete, A.R., Zarco-Tejada, P., Lee, J.-E., Moran, M.S., Ponce-Campos, G., Beer, C., Camps-Valls, G., Buchmann, N., Gianelle, D., Klumpp, K., Cescatti, A., Baker, J.M., Griffis, T.J., 2014. Global and time-resolved monitoring of crop photosynthesis with chlorophyll fluorescence. Proc. Natl. Acad. Sci. 111, E1327–E1333. https://doi.org/10.1073/pnas.1320008111

Holder, C.D., 2012. The relationship between leaf hydrophobicity , water droplet retention , and leaf angle of common species in a semi-arid region of the western United States. Agric. For. Meteorol. 152, 11–16. https://doi.org/10.1016/j.agrformet.2011.08.005

Homer, C., Dewitz, J., Yang, L., Jin, S., Danielson, P., Xian, G., Coulston, J., Herold, N., Wickham, J., Megown, K., 2015. Completion of the 2011 National Land Cover Database for the Conterminous United States – Representing a Decade of Land Cover Change Information. Photogrammetric Engineering and Remote Sensing, 81, 345-354. https://doi.org/10.14358/PERS.81.5.345

Joiner, J., Guanter, L., Lindstrot, R., Voigt, M., Vasilkov, A.P., Middleton, E.M., Huemmrich, K.F., Yoshida, Y., Frankenberg, C., 2013. Global monitoring of terrestrial chlorophyll fluorescence from moderate-spectral-resolution near-infrared satellite measurements: methodology, simulations, and application to GOME-2. Atmos. Meas. Tech. 6, 2803–2823. https://doi.org/10.5194/amt-6-2803-2013

Joiner, J., Yoshida, Y., Vasilkov, A.P., Middleton, E.M., Campbell, P.K.E., Yoshida, Y., Kuze, A., Corp, L.A., 2012. Filling-in of near-infrared solar lines by terrestrial fluorescence and other geophysical effects: Simulations and space-based observations from SCIAMACHY and GOSAT. Atmos. Meas. Tech. 5, 809–829. https://doi.org/10.5194/amt-5-809-2012

Joiner, J., Yoshida, Y., Vasilkov, A.P., Yoshida, Y., Corp, L.A., Middleton, E.M., 2011. First observations of global and seasonal terrestrial chlorophyll fluorescence from space. Biogeosciences 8, 637–651. https://doi.org/10.5194/bg-8-637-2011

Joo, E., Hussain, M.Z., Zeri, M., Masters, M.D., Miller, J.N., Gomez-casanovas, N., Delucia, E.H., 2016. The influence of drought and heat stress on long-term carbon fluxes of bioenergy crops grown in the Midwestern USA. Plant Cell Environ. 39, 1928–1940. https://doi.org/10.1111/pce.12751

Khatami, R., & Mountrakis, G. (2012). Implications of classification of methodological decisions in flooding analysis fromhurricane Katrina. Remote Sensing, 4(12), 3877–3891

Kobayashi, H., Iwabuchi, H., 2008. A coupled 1-D atmosphere and 3-D canopy radiative transfer model for canopy reflectance, light environment, and photosynthesis simulation in a heterogeneous landscape. Remote Sensing of Environment, 112, 173–185. https://doi.org/10.1016/j.rse.2007.04.010

Köhler, P., Frankenberg, C., Magney, T.S., Guanter, L., Joiner, J., Landgraf, J., 2018. Global retrievals of solar induced chlorophyll fluorescence with TROPOMI: first results and inter-sensor comparison to OCO-2. Geophys. Res. Lett. 45, 456–463. https://doi.org/10.1029/2018GL079031

Köhler, P., Guanter, L., Joiner, J., 2015. A linear method for the retrieval of sun-induced chlorophyll fluorescence from GOME-2 and SCIAMACHY data. Atmos. Meas. Tech. 8, 2589–2608. https://doi.org/10.5194/amt-8-2589-2015

Li, X., Xiao, J., 2019. A Global, 0.05-Degree Product of Solar-Induced Chlorophyll Fluorescence Derived from OCO-2, MODIS, and Reanalysis Data. Remote Sens. 11, 517. https://doi.org/10.3390/rs11050517

Li, X., Xiao, J., He, B., 2018a. Chlorophyll fluorescence observed by OCO-2 is strongly related to gross primary productivity estimated from flux towers in temperate forests. Remote Sens. Environ. 204, 659–671. https://doi.org/10.1016/j.rse.2017.09.034

Li, X., Xiao, J., He, B., 2018b. Higher absorbed solar radiation partly offset the negative effects of water stress on the photosynthesis of Amazon forests during the 2015 drought. Environ. Res. Lett. 13, 044005. https://doi.org/10.1088/1748-9326/aab0b1

Li, X., Xiao, J., He, B., Altaf Arain, M., Beringer, J., Desai, A.R., Emmel, C., Hollinger, D.Y., Krasnova, A., Mammarella, I., Noe, S.M., Ortiz, P.S., Rey-Sanchez, A.C., Rocha, A. V., Varlagin, A., 2018c. Solar-induced chlorophyll fluorescence is strongly correlated with terrestrial photosynthesis for a wide variety of biomes: First global analysis based on OCO-2 and flux tower observations. Glob. Chang. Biol. 24, 3990–4008. https://doi.org/10.1111/gcb.14297

Liu, X., Guanter, L., Liu, L., Damm, A., Malenovský, Z., Rascher, U., Peng, D., Du, S., Gastellu-Etchegorry, J.P., 2018. Downscaling of solar-induced chlorophyll fluorescence from canopy level to photosystem level using a random forest model. Remote Sens. Environ. https://doi.org/10.1016/j.rse.2018.05.035

Lu, X., Cheng, X., Li, X., Tang, J., 2018. Opportunities and challenges of applications of satellite-derived sun-induced fluorescence at relatively high spatial resolution. Sci. Total Environ. 619–620, 649–653. https://doi.org/10.1016/j.scitotenv.2017.11.158

MacBean, N., Maignan, F., Bacour, C., Lewis, P., Peylin, P., Guanter, L., Köhler, P., Gómez-Dans, J., Disney, M., 2018. Strong constraint on modelled global carbon uptake using solar-induced chlorophyll fluorescence data. Sci. Rep. 8, 1–12. https://doi.org/10.1038/s41598-018-20024-w

Miao, G., Guan, K., Yang, X., Bernacchi, C.J., Berry, J.A., DeLucia, E.H., Wu, J., Moore, C.E., Meacham, K., Cai, Y., Peng, B., Kimm, H., Masters, M.D., 2018. Sun-Induced Chlorophyll Fluorescence, Photosynthesis, and Light Use Efficiency of a Soybean Field from Seasonally Continuous Measurements. J. Geophys. Res. Biogeosciences 123, 610–623. https://doi.org/10.1002/2017JG004180

Migliavacca, M., Perez-Priego, O., Rossini, M., El-Madany, T.S., Moreno, G., van der Tol, C., Rascher, U., Berninger, A., Bessenbacher, V., Burkart, A., Carrara, A., Fava, F., Guan, J.H., Hammer, T.W., Henkel, K., Juarez-Alcalde, E., Julitta, T., Kolle, O., Martín, M.P., Musavi, T., Pacheco-Labrador, J., Pérez-Burgueño, A., Wutzler, T., Zaehle, S., Reichstein, M., 2017. Plant functional traits and canopy structure control the relationship between photosynthetic CO2uptake and far-red sun-induced fluorescence in a Mediterranean grassland under different nutrient availability. New Phytol. 214, 1078–1091. https://doi.org/10.1111/nph.14437

Monteith, J.L., 1972. Solar Radiation and Productivity in Tropical Ecosystems. J. Appl. Ecol.

9, 747. https://doi.org/10.2307/2401901

Myneni, R., Hoffman, Y., Knyazikhin, 2002. Global products of vegetation leaf area and fraction absorbed PAR from one year of MODIS data. Remote Sensing of. Environment 76, 139–155. https://doi.org/10.1016/S0034-4257(02)00074-3

Myneni, R., Knyazkhin, Y. (2018). VIIRS/NPP Leaf Area Index/FPAR 8-Day L4 Global 500m SIN Grid V001 [Data set]. NASA EOSDIS Land Processes DAAC. doi: 10.5067/VIIRS/VNP15A2H.001

Ollinger, S. V., Richardson, A. D., Martin, M. E., Hollinger, D. Y., Frolking, S. E., Reich, P. B.,et al. (2008). Canopy nitrogen, carbon assimilation, and albedo in temperate and borealforests: Functional relations and potential climate feedbacks. Proceedings of theNational Academy of Sciences of the United States of America, 105, 19336–19341.

Oosterhuis, D.M., Walker, S., Eastham, J., 1985. Soybean Leaflet Movements as an Indicator of Crop Water Stress. Crop Science. 25, 1101–1106. https://doi.org/10.2135/cropsci1985.0011183X002500060048x

Peng, D., Zhang, B., Liu, L., Fang, H., Chen, D., Hu, Y., Liu, L., 2012. Characteristics and drivers of global NDVI-based FPAR from 1982 to 2006 26, 1–15. https://doi.org/10.1029/2011GB004060

Porcar-castell, A., Tyystjärvi, E., Atherton, J., Tol, C. Van Der, Flexas, J., Pfündel, E.E., Moreno, J., Frankenberg, C., Berry, J.A., 2014. Linking chlorophyll a fluorescence to photosynthesis for remote sensing applications : mechanisms and challenges 65, 4065–4095. https://doi.org/10.1093/jxb/eru191

Romero, J.M., Cordon, G.B., Lagorio, M.G., 2018. Modeling re-absorption of fluorescence from the leaf to the canopy level. Remote Sens. Environ. 204, 138–146. https://doi.org/10.1016/j.rse.2017.10.035

Ryu, Y., Jiang, C., Kobayashi, H., Detto, M., 2018. MODIS-derived global land products of shortwave radiation and diffuse and total photosynthetically active radiation at 5 km resolution from 2000. Remote Sens. Environ. 204, 812–825. https://doi.org/10.1016/j.rse.2017.09.021

Shiga, Y.P., Tadić, J.M., Qiu, X., Yadav, V., Andrews, A.E., Berry, J.A., Michalak, A.M., 2018. Atmospheric CO2 observations reveal strong correlation between regional net biospheric carbon uptake and solar-induced chlorophyll fluorescence. Geophys. Res. Lett. 45, 1122–1132. https://doi.org/10.1002/2017GL076630

Smith, W.K., Biederman, J.A., Scott, R.L., Moore, D.J.P., He, M., Kimball, J.S., Yan, D., Hudson, A., Barnes, M.L., MacBean, N., Fox, A.M., Litvak, M.E., 2018. Chlorophyll Fluorescence Better Captures Seasonal and Interannual Gross Primary Productivity Dynamics Across Dryland Ecosystems of Southwestern North America. Geophys. Res. Lett. 45, 748–757. https://doi.org/10.1002/2017GL075922

Song, L., Guanter, L., Guan, K., You, L., Huete, A., Ju, W., Zhang, Y., 2018. Satellite sun-induced chlorophyll fluorescence detects early response of winter wheat to heat stress in the Indian Indo-Gangetic Plains. Glob. Chang. Biol. 24, 4023–4037. https://doi.org/10.1111/gcb.14302

Sun, Y., Frankenberg, C., Jung, M., Joiner, J., Guanter, L., Köhler, P., Magney, T., 2018. Overview of Solar-Induced chlorophyll Fluorescence (SIF) from the Orbiting Carbon Observatory-2: Retrieval, cross-mission comparison, and global monitoring for GPP. Remote Sens. Environ. 209, 808–823. https://doi.org/10.1016/j.rse.2018.02.016

Sun, Y., Fu, R., Dickinson, R., Joiner, J., Frankenberg, C., Gu, L., Xia, Y., Fernando, N., 2015. Drought onset mechanisms revealed by satellite solar-induced chlorophyll fluorescence: Insights from two contrasting extreme events. J. Geophys. Res. Biogeosciences 120, 2427–2440. https://doi.org/10.1002/2015JG003150

Suyker, A.E., Verma, S.B., 2012. Gross primary production and ecosystem respiration of irrigated and rainfed maize – soybean cropping systems over 8 years. Agricultural and Forest Meteorology. 165, 12–24. https://doi.org/10.1016/j.agrformet.2012.05.021

Tian, Y., 2004. Comparison of seasonal and spatial variations of leaf area index and fraction of absorbed photosynthetically active radiation from Moderate Resolution Imaging Spectroradiometer (MODIS) and Common Land Model. J. Geophys. Res. 109, D01103. https://doi.org/10.1029/2003JD003777

USDA Foreign Agricultural Service (December 2018) World Agricultural Production, Circular Ser WAP 12-18, pp. 17-24.

Verma, M., Schimel, D., Evans, B., Frankenberg, C., Beringer, J., Drewry, D.T., Magney, T., Marang, I., Hutley, L., Moore, C., Eldering, A., 2017. Effect of environmental conditions on the relationship between solar-induced fluorescence and gross primary productivity at an OzFlux grassland site. J. Geophys. Res. Biogeosciences 122, 716–733. https://doi.org/10.1002/2016JG003580

Verrelst, J., Rivera, J.P., van der Tol, C., Magnani, F., Mohammed, G., Moreno, J., 2015. Global sensitivity analysis of the SCOPE model: What drives simulated canopy-leaving sun-induced fluorescence? Remote Sens. Environ. 166, 8–21. https://doi.org/10.1016/j.rse.2015.06.002

Wang, C., Chen, J., Wu, J., Tang, Y., Shi, P., Black, T.A., Zhu, K., 2017. A snow-free vegetation index for improved monitoring of vegetation spring green-up date in deciduous ecosystems. Remote Sens. Environ. 196, 1–12. https://doi.org/10.1016/j.rse.2017.04.031

Wood, J.D., Griffis, T.J., Baker, J.M., Frankenberg, C., Verma, M., Yuen, K., 2017. Multiscale analyses of solar-induced fluorescence and gross primary production. Geophys. Res. Lett. 44, 533–541. https://doi.org/10.1002/2016GL070775

Xu, S., Liu, Z., Zhao, L., Zhao, H., Ren, S., 2018. Diurnal response of sun-induced fluorescence and PRI to water stress in maize using a near-surface remote sensing platform. Remote Sens. 10, 1510. https://doi.org/10.3390/rs10101510

Yan, K., Park, T., Yan, G., Liu, Z., Yang, B., Chen, C., Nemani, R.R., Knyazikhin, Y., Myneni, R.B., 2016. Evaluation of MODIS LAI / FPAR Product Collection 6 . Part 2 : Validation and Intercomparison. Remote Sens. 8, 460. https://doi.org/10.3390/rs8060460

Yang, H., Yang, X., Zhang, Y., Heskel, M.A., Lu, X., Munger, J.W., Sun, S., Tang, J., 2017. Chlorophyll fluorescence tracks seasonal variations of photosynthesis from leaf to canopy in a temperate forest. Glob. Chang. Biol. 23, 2874–2886. https://doi.org/10.1111/gcb.13590

Yang, K., Ryu, Y., Dechant, B., Berry, J.A., Hwang, Y., Jiang, C., Kang, M., Kim, J., Kimm, H., Kornfeld, A., Yang, X., 2018. Sun-induced chlorophyll fluorescence is more strongly related to absorbed light than to photosynthesis at half-hourly resolution in a rice paddy. Remote Sens. Environ. 216, 658–673. https://doi.org/10.1016/j.rse.2018.07.008

Yang, P., van der Tol, C., 2018. Linking canopy scattering of far-red sun-induced chlorophyll fluorescence with reflectance. Remote Sens. Environ. 209, 456–467. https://doi.org/10.1016/j.rse.2018.02.029

Yang, X., Tang, J., Mustard, J.F., Lee, J., Rossini, M., 2015. Solar-induced chlorophyll fluorescence correlates with canopy photosynthesis on diurnal and seasonal scales in a temperate deciduous forest. Geophys. Res. Lett. 42, 2977–2987. https://doi.org/10.1002/2015GL063201

Yoshida, Y., Joiner, J., Tucker, C., Berry, J., Lee, J.E., Walker, G., Reichle, R., Koster, R., Lyapustin, A., Wang, Y., 2015. The 2010 Russian drought impact on satellite measurements of solar-induced chlorophyll fluorescence: Insights from modeling and comparisons with parameters derived from satellite reflectances. Remote Sens. Environ. 166, 163–177. https://doi.org/10.1016/j.rse.2015.06.008

Zeng, Y., Badgley, G., Dechant, B., Ryu, Y., Chen, M., Berry, J.A., 2019. Apratical approach for estimation the escape ratio of near-infrared solar-induced chlorophyll fluorescence. Remote Sens. Environ. 232, 111209. https://doi.org/10.1016/j.rse.2019.05.028

Zhang, Y., Guanter, L., Berry, J.A., Joiner, J., van der Tol, C., Huete, A., Gitelson, A., Voigt, M., Köhler, P., 2014. Estimation of vegetation photosynthetic capacity from space-based measurements of chlorophyll fluorescence for terrestrial biosphere models. Glob. Chang. Biol. 20, 3727–3742. https://doi.org/10.1111/gcb.12664

Zhang, Y., Guanter, L., Berry, J.A., van der Tol, C., Yang, X., Tang, J., Zhang, F., 2016. Model-based analysis of the relationship between sun-induced chlorophyll fluorescence and gross primary production for remote sensing applications. Remote Sens. Environ. 187, 145–155. https://doi.org/10.1016/j.rse.2016.10.016

Zhang, Y., Joiner, J., Alemohammad, S.H., Zhou, S., Gentine, P., 2018. A global spatially Continuous Solar Induced Fluorescence (CSIF) dataset using neural networks. Biogeosciences 15, 5779–5800. https://doi.org/10.5194/bg-15-5779-2018

Zhang, Z., Zhang, Y., Joiner, J., Migliavacca, M., 2018. Angle matters : Bidirectional effects impact the slope of relationship between gross primary productivity and sun ‐ induced chlorophyll fluorescence from Orbiting Carbon Observatory ‐ 2 across biomes. Global Biogeochem. Cycles 24, 5017–5020. https://doi.org/10.1111/gcb.14427

Zuromski, L.M., Bowling, D.R., Köhler, P., Frankenberg, C., Goulden, M.L., Blanken, P.D., Lin, J.C., 2018. Solar-Induced Fluorescence Detects Interannual Variation in Gross Primary Production of Coniferous Forests in the Western United States. Geophys. Res.

Lett. 45, 7184–7193. https://doi.org/10.1029/2018GL077906

Glossary:

SIF: solar-induced chlorophyll fluorescence

$\mathrm{SIF}_{\mathrm{inst}}$: instantaneous solar-induced chlorophyll fluorescence

$\mathrm{SIF}_{\mathrm{par}}$: $\mathrm{SIF}_{\mathrm{inst}}$ normalized by PAR

$\mathrm{SIF}_{\mathrm{yield\ apparent}}$: apparent canopy SIF yield, defined as SIF observed in the direction of the sensor per PAR absorbed by canopies, is a product of fluorescence yield and the escaping ratio.

Φ_{F}: fluorescence yield

f^{esc}: the escaping ratio, which can be calculated as NIRv/fPAR

GPP: gross primary production

LUE: light use efficiency of GPP

PAR: photosynthetically active radiation

fPAR: the fraction of absorbed photosynthetically active radiation

APAR: absorbed photosynthetically active radiation

NIRv: the near-infrared reflectance of vegetation, which can be calculated as NDVI*NIR

NIR: the reflectance of near-infrared band

NDVI: normalized difference vegetation index

LAI: leaf area index

LAD: leaf angle distribution

Declaration of competing interests

☒ The authors declare that they have no known competing financial interests or personal relationships that could have appeared to influence the work reported in this paper.

☐The authors declare the following financial interests/personal relationships which may be considered as potential competing interests:

Author Statement

Cong Wang: Conceptualization, Methodology, Software, Formal analysis, Investigation, Writing - Original Draft, Writing – Review & Editing, Visualization**. Kaiyu Guan:** Conceptualization, Methodology, Writing - Original Draft, Writing – Review & Editing, Supervision, Funding acquisition. **Bin Peng:** Conceptualization, Methodology, Writing - Original Draft, Writing – Review & Editing**. Min Chen:** Conceptualization, Writing - Original Draft. **Chongya Jiang:** Writing - Original Draft, Writing – Review & Editing. **Yelu Zeng:** Methodology, Writing – Review & Editing. **Genghong Wu:** Formal analysis, Writing – Review & Editing. **Sheng Wang:** Writing – Review & Editing. **Jin Wu:** Conceptualization, Writing - Original Draft. **Xi Yang:** Writing - Original Draft, Writing. **Christian Frankenberg:** Resource, Writing - Original Draft. **Philipp Köhler:** Resource, Writing - Original Draft. **Joseph Berry:** Conceptualization. **Carl Bernacchi:** Writing - Original Draft. **Kai Zhu:** Writing - Original Draft. **Caroline Alden:** Writing - Original Draft, Writing – Review & Editing**. Guofang Miao:** Conceptualization.

Highlights

- $SIF_{yield\ apparent}$ is interpreted using high spatial resolution satellite footprints.
- Different spatio-temporal patterns of $SIF_{yield\ apparent}$ are revealed among vegetation types.
- $SIF_{yield\ apparent}$ of croplands is larger than non-croplands in summer.
- Escaping ratio largely explains the variations of $SIF_{yield\ apparent}$ in the Midwest.
- Spatial variability of $SIF_{yield\ apparent}$ is correlated to precipitation.